

## Synchronous behaviors of three coupled liquid crystal elastomer-based spring oscillators under linear temperature fields

Haiyang Wu, Biao Zhang, and Kai Li <sup>\*</sup>*School of Civil Engineering, Anhui Jianzhu University, Hefei, Anhui 230601, China*

(Received 21 November 2023; accepted 8 January 2024; published 5 February 2024)

Self-oscillating coupled systems possess the ability to actively absorb external environmental energy to sustain their motion. This quality endows them with autonomy and sustainability, making them have application value in the fields of synchronization and clustering, thereby furthering research and exploration in these domains. Building upon the foundation of thermal responsive liquid crystal elastomer-based (LCE-based) spring oscillators, a synchronous system comprising three LCE-based spring oscillators interconnected by springs is established. In this paper, the synchronization phenomenon is described, and the self-oscillation mechanism is revealed. The results indicate that by varying system parameters and initial conditions, three synchronization patterns emerge, namely, full synchronous mode, partial synchronous mode, and asynchronous mode. For strongly interacting systems, full synchronous mode always prevails, while for weak interactions, the adjustment of initial velocities in magnitude and direction yields the three synchronization patterns. Additionally, this study explores the impact of several system parameters, including LCE elasticity coefficient and spring elasticity coefficient, on the amplitude, frequency, and synchronous mode of the system. The findings in this paper can enhance our understanding of the synchronization behavior of multiple mutually coupled LCE-based spring oscillators, with promising applications in energy harvesting, soft robotics, signal monitoring, and various other fields.

DOI: [10.1103/PhysRevE.109.024701](https://doi.org/10.1103/PhysRevE.109.024701)

### I. INTRODUCTION

Self-oscillation system refers to a system that can exhibit sustained periodic motion through obtaining energy from an external steady environment [1–5]. Self-oscillation is ubiquitous in nature, manifesting in various phenomena such as the rhythmic beating of the heart and the swaying of a swing. One of the key advantages of self-excited oscillation is its ability to operate without the need for additional controllers, drawing energy from the surrounding environment to sustain its self-sustained oscillatory behavior [6,7]. This unique characteristic holds significant promise in a wide range of applications, including medical devices [8,9], soft robotics [10,11], actuators [12–14], and energy harvesting [15,16].

In recent years, as active materials have been the subject of extensive research, self-oscillating systems based on active materials, such as ionic gels [17,18], hydrogels [19], photothermal responsive polymer [20–26], shape memory polymers [27], and dielectric elastomers [28], have been continuously developed. These active materials exhibit diverse responses to light [29,30], heat [31,32], electric field [33], and magnetic field [34,35], including changes in shape and motion. A variety of self-oscillating modes based on active materials are constructed, including rolling [36,37], jumping [38], twisting [39], buckling [40,41], bending [42,43], swinging [44], vibrating [45], curling [46], stretching [47], shuttling [48], spinning [49], and floating [50]. Liquid crystal elastomer (LCE) is a kind of material with superior properties [51–54],

which forms a polymer network structure through the cross-linking of liquid crystal monomer molecules [55]. When the LCE is exposed to external stimuli such as light [36,45,46,49], heat [31,32], electricity [33], and magnetism [35], reversible morphological changes can occur. LCE possesses the benefits of fast response and extensive deformation, rendering it more apt for constructing self-oscillation systems. Presently, extensive experimental and theoretical research has been conducted on self-oscillation based on LCE.

Synchronization is ubiquitous in nature, such as fireflies, the pendulum, and the contraction of the heart [56–60]. And the synchronous phenomenon is put forward for the first time in the 17th century, when Huygens observed during one voyage that two pendulums connected by a beam can reverse synchronous vibration, and discovered that the cause of the reverse sync between the two pendulums was the tiny vibrations propagated by the beam [61,62]. Based on this phenomenon, he put forward the theory of synchronization. On the basis of Huygens' research, scientists have done a lot of research on the phenomenon of synchronization, such as quantum mechanical synchronization, explosion synchronization, synchronization nonlinear system [63–65], etc. These synchronizations provide the foundation theory for the establishment of a large range of synchronization models and neural networks [66–68].

Nowadays, a lot of self-oscillating systems are established based on LCE materials, most of which are about a single self-oscillator, while a few studied the interaction of multiple spontaneous oscillators [69,70]. To achieve a wider range of applications, we propose a coupling system that consists of three LCE-based spring oscillators under a linear temperature

\*Corresponding author: [kli@ahjzu.edu.cn](mailto:kli@ahjzu.edu.cn)

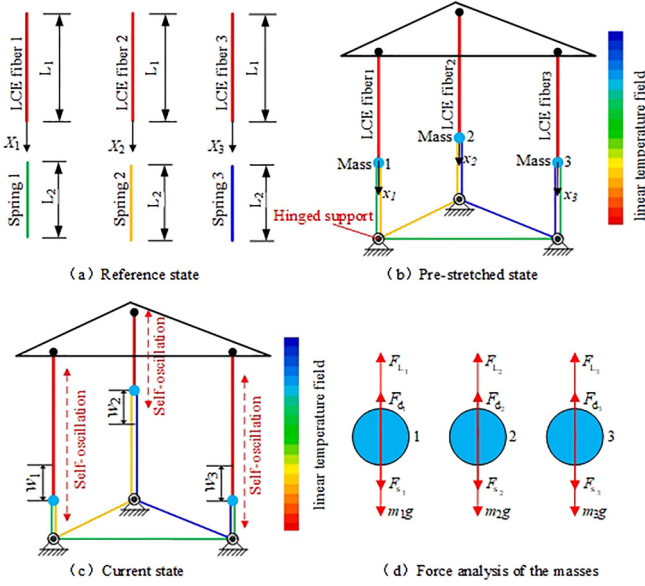


FIG. 1. Schematic diagram of self-oscillating coupled system. (a) Reference state; (b) prestretched state; (c) current state; (d) force analysis of the masses.

field. Then we describe the phenomena of self-oscillation and synchronization, revealing the mechanism of self-oscillation. This study is valuable for designing more self-sustained synchronization systems utilizing diverse thermally responsive materials [71], which have broad applications in fields such as soft robotics, energy harvesters, sensors, and so on.

The structure of the paper is as follows. In Sec. II, based on the dynamic LCE model, the governing equations of a coupled system of three LCE-based spring oscillators are derived. In Sec. III, three synchronization modes are described, and the self-oscillation mechanism is revealed. In Secs. IV–VI, we quantitatively investigate the influence of system parameters on self-oscillation. Finally, in Sec. VII, we provide a summary.

## II. MODEL AND FORMULATION

In this section, we first construct a synchronous self-oscillating system coupled by three LCE-based spring oscillators under a linear temperature field. Then, we derive and linearize the governing equations of the coupled synchronous system.

### A. Dynamic model of three LCE-based spring oscillators

In this section, we formulate a dynamical model for the LCE-based spring oscillators under a linear temperature field. Figure 1 illustrates the model of the self-oscillating coupled system under a linear temperature field. The system comprises three LCE-based spring oscillators interconnected by springs. In the initial state, the original length of each LCE fiber is  $L_0$  and the original length of each spring is  $L_S$ , as drawn in Fig. 1(a). Initially, one end of every LCE fiber is anchored, while the opposite end is attached to a spring. This lower section of the spring is linked to another spring through a pulley, thereby effectively connecting three spring oscillators. To ensure the force balance of the system, the LCE fibers

and the springs are required to be prestretched, where the prestretched amount of each LCE fiber and each spring is  $\lambda_1$  and  $\lambda_2$ . It can be seen in Fig. 1(b) that in equilibrium, the length of each LCE fiber is  $\lambda_1 L_0$  and the length of each spring is  $\lambda_2 L_S$ . The governing equations of the coupled system in the initial state are

$$\begin{aligned} m_1 g + F_{s_{10}} - F_{L_{10}} &= 0, \\ m_2 g + F_{s_{20}} - F_{L_{20}} &= 0, \\ m_3 g + F_{s_{30}} - F_{L_{30}} &= 0, \end{aligned} \quad (1)$$

where  $F_{s_{10}}$ ,  $F_{s_{20}}$ , and  $F_{s_{30}}$  are the initial elastic forces of the springs and  $F_{L_{10}}$ ,  $F_{L_{20}}$ , and  $F_{L_{30}}$  are the initial elastic forces of the LCE fibers, where  $F_{s_0} = k(\lambda_2 L_S - L_S)$  and  $F_{L_0} = K(\lambda_1 L_0 - L_0)$ , while  $k$  and  $K$  are the spring elastic coefficient and the LCE elastic coefficient. From this, the relationship between  $\lambda_1$  and  $\lambda_2$  can be obtained, i.e.,

$$\lambda_2 = \frac{\bar{K}(\lambda_1 - 1) - 1}{\bar{k}\bar{L}_2} + 1, \quad (2)$$

where  $\bar{F}_{s_{10}} = F_{s_{10}}/mg$ ,  $\bar{F}_{s_{20}} = F_{s_{20}}/mg$ ,  $\bar{F}_{s_{30}} = F_{s_{30}}/mg$ ,  $\bar{F}_{L_{10}} = F_{L_{10}}/mg$ ,  $\bar{F}_{L_{20}} = F_{L_{20}}/mg$ ,  $\bar{F}_{L_{30}} = F_{L_{30}}/mg$ ,  $\bar{k} = kL_1/mg$ ,  $\bar{K} = KL_1/mg$ , and  $\bar{L}_2 = L_2/L_1$ .

It can be seen from Fig. 1(c) that after heating, the LCE fibers begin to oscillate in the direction of fiber length, in which the displacements of the masses are  $w_1(t)$ ,  $w_2(t)$ , and  $w_3(t)$ . The force analysis of the three fibers as shown in Fig. 1(d), where  $F_{s_1}$ ,  $F_{s_2}$ , and  $F_{s_3}$  are the elastic force of the springs and  $F_{L_1}$ ,  $F_{L_2}$ , and  $F_{L_3}$  are the elastic force of LCE fibers.  $F_{d_1}$ ,  $F_{d_2}$ , and  $F_{d_3}$  are the damping force. For simplicity, we assume that the damping force is linearly related to velocity and consistently opposes the motion of the fiber. The equations that describe the system can be formulated as

$$\begin{aligned} m_1 \ddot{w}_1(t) - m_1 g - F_{s_1}(t) + F_{L_1}(t) + F_{d_1}(t) &= 0, \\ m_2 \ddot{w}_2(t) - m_2 g - F_{s_2}(t) + F_{L_2}(t) + F_{d_2}(t) &= 0, \\ m_3 \ddot{w}_3(t) - m_3 g - F_{s_3}(t) + F_{L_3}(t) + F_{d_3}(t) &= 0, \end{aligned} \quad (3)$$

where  $\ddot{w}_1(t)$ ,  $\ddot{w}_2(t)$ , and  $\ddot{w}_3(t)$  are the accelerations  $\frac{d^2 w_1(t)}{dt^2}$ ,  $\frac{d^2 w_2(t)}{dt^2}$ , and  $\frac{d^2 w_3(t)}{dt^2}$ , and the elastic force of the spring is

$$\begin{aligned} F_{s_1} &= k[\lambda_2 L_S - L_S - w_1(t)] - k[w_1(t) + w_2(t)] \\ &\quad - k[w_1(t) + w_3(t)], \\ F_{s_2} &= k[\lambda_2 L_S - L_S - w_2(t)] - k[w_2(t) + w_1(t)] \\ &\quad - k[w_2(t) + w_3(t)], \\ F_{s_3} &= k[\lambda_2 L_S - L_S - w_3(t)] - k[w_3(t) + w_1(t)] \\ &\quad - k[w_3(t) + w_2(t)]. \end{aligned} \quad (4)$$

We assume nonlinear damping for the damping characteristics, and it can be written as

$$\begin{aligned} F_{d_1} &= (a_0 + a_1 |\dot{w}_1|) \dot{w}_1, \\ F_{d_2} &= (a_0 + a_1 |\dot{w}_2|) \dot{w}_2, \\ F_{d_3} &= (a_0 + a_1 |\dot{w}_3|) \dot{w}_3, \end{aligned} \quad (5)$$

where  $a_0$  and  $a_1$  are the first damping coefficient and the second damping coefficient, and  $\dot{w}_1(t)$ ,  $\dot{w}_2(t)$ , and  $\dot{w}_3(t)$  are the velocities  $\frac{dw_1(t)}{dt}$ ,  $\frac{dw_2(t)}{dt}$ , and  $\frac{dw_3(t)}{dt}$ .

### B. Tension of the LCE fiber

Since the nonuniform deformation of the LCE fibers under a linear temperature field, a Lagrangian coordinate system  $X$ , and a Euler coordinate system  $x$  are established as shown in Figs. 1(a) and 1(b). The instantaneous position of the particle is  $x_i = x_i(X_i, t)$  ( $i = 1, 2, 3$ ), and the displacement of the particle is  $u_i(X_i, t)$  ( $i = 1, 2, 3$ ) during the LCE fibers oscillating.

There is an assumption that the tension is directly proportional to the strain of the LCE fiber, following a linear dependency:

$$\begin{aligned} F_{L_1} &= KL_1[\varepsilon_1(X, t) - \varepsilon_T(X, t)], \\ F_{L_2} &= KL_2[\varepsilon_2(X, t) - \varepsilon_T(X, t)], \\ F_{L_3} &= KL_3[\varepsilon_3(X, t) - \varepsilon_T(X, t)], \end{aligned} \quad (6)$$

where  $K$  is the LCE elastic coefficient, and the one-dimensional strains  $\varepsilon_1(X, t)$ ,  $\varepsilon_2(X, t)$ , and  $\varepsilon_3(X, t)$  are given by

$$\begin{aligned} \varepsilon_1(X, t) &= \frac{\partial u_1(X, t)}{\partial X_1}, \\ \varepsilon_2(X, t) &= \frac{\partial u_2(X, t)}{\partial X_2}, \\ \varepsilon_3(X, t) &= \frac{\partial u_3(X, t)}{\partial X_3}. \end{aligned} \quad (7)$$

Moreover, the heat-induced strain  $\varepsilon_T(X, t)$  is directly proportional to the temperature difference  $T(X, t)$ :

$$\varepsilon_T(X, t) = \alpha T(X, t), \quad (8)$$

where  $\alpha$  is the thermal expansion coefficient,  $\alpha < 0$  indicates thermal contraction, and  $\alpha > 0$  denotes thermal expansion.

Given the uniform and constant of the driving force  $F_L(t)$  in the LCE fiber, we can calculate it by integrating both sides of Eq. (6) from 0 to  $X$ . Combining this with Eqs. (7) and (8), we can derive the driving force at the end of the LCE fiber:

$$\begin{aligned} F_{L_1}(t) &= K \left[ w_1(t) - \alpha \int_0^L T(X, t) dX \right], \\ F_{L_2}(t) &= K \left[ w_2(t) - \alpha \int_0^L T(X, t) dX \right]. \end{aligned} \quad (9)$$

Because the temperature field within the LCE fiber is nonuniform and varies over time, heat exchange occurs between the fiber and its surroundings, resulting in a temperature distribution denoted as  $T_{\text{ext}}(t)$ . Therefore, there is an assumption that the radius of the fiber is significantly smaller than the length  $L$ , so the temperature field in the LCE fiber can be seen as uniform, namely,  $T = T(X, t)$ . In this case, the temperature field in the LCE fiber is as follows:

$$\tau \frac{dT(X, t)}{dt} = T_{\text{ext}}(x) - T(X, t), \quad (10)$$

where the characteristic time  $\tau = \frac{\rho_c}{h}$ ,  $\rho_c$  is the heat capacity and  $h$  is the heat transfer coefficient. There is an assumption that the temperature field in the environment follows a linear pattern:

$$T_{\text{ext}}(x) = \beta x + Q, \quad (11)$$

where  $Q$  represents the temperature at  $x = 0$  and  $\beta$  indicates the temperature gradient.

We introduce the following dimensionless parameters:  $\bar{t} = t/\sqrt{L/g}$ ,  $\bar{F}_L = F_L/mg$ ,  $\bar{u} = u/L$ ,  $\bar{w} = w/L$ ,  $\bar{X} = X/L$ ,  $\bar{x} = x/l$ ,  $\bar{\tau} = \tau/\sqrt{L/g}$ ,  $\bar{K} = KL/mg$ ,  $\bar{\alpha} = \alpha T_L$ ,  $\bar{T} = T/T_L$ ,  $\bar{T}_{\text{ext}} = T_{\text{ext}}/T_L$ ,  $\bar{\beta} = \beta L/T_L$ , and  $\bar{Q} = Q/T_L$  ( $T_L$  denotes the temperature at  $x = L$ ).

In this case, the elastic force of LCE fiber can be written as

$$\begin{aligned} \bar{F}_{L_1} &= \bar{K} \left[ \bar{w}_1(\bar{t}) - \bar{\alpha} \int_0^1 \bar{T}(\bar{X}_1, \bar{t}) d\bar{X} \right], \\ \bar{F}_{L_2} &= \bar{K} \left[ \bar{w}_2(\bar{t}) - \bar{\alpha} \int_0^1 \bar{T}(\bar{X}_2, \bar{t}) d\bar{X} \right]. \end{aligned} \quad (12)$$

The temperature field's solution is as follows:

$$\begin{aligned} \bar{T}(\bar{X}, \bar{t}) &= \frac{\bar{\beta}[\bar{w}(\bar{t}) + 1]}{e^{\bar{\alpha}\bar{\beta}} - 1} (e^{\bar{\alpha}\bar{\beta}\bar{X}} - 1) + \bar{Q} + \bar{\tau} \frac{\bar{\beta}\dot{\bar{w}}(\bar{t})}{e^{\bar{\alpha}\bar{\beta}} - 1} \\ &\quad \times \left[ \frac{(e^{\bar{\alpha}\bar{\beta}\bar{X}} - 1)(\bar{\alpha}\bar{\beta}e^{\bar{\alpha}\bar{\beta}} - e^{\bar{\alpha}\bar{\beta}} + 1)}{e^{\bar{\alpha}\bar{\beta}} - 1} - \bar{\alpha}\bar{\beta}\bar{X}e^{\bar{\alpha}\bar{\beta}\bar{X}} \right]. \end{aligned} \quad (13)$$

By inserting Eq. (13) into Eq. (12), the elastic force  $\bar{F}_L(t)$  of LCE fiber can be written as

$$\begin{aligned} \bar{F}_{L_1}(\bar{t}) &= \frac{\bar{K}\bar{\alpha}\bar{\beta}}{e^{\bar{\alpha}\bar{\beta}} - 1} \bar{w}_1(\bar{t}) + \bar{K}\bar{\alpha}\bar{\beta}\bar{\tau} \frac{1 - e^{\bar{\alpha}\bar{\beta}} + \bar{\alpha}\bar{\beta}e^{\bar{\alpha}\bar{\beta}}}{(e^{\bar{\alpha}\bar{\beta}} - 1)^2} \dot{w}_1(t) \\ &\quad + \bar{K} \left( \frac{\bar{\alpha}\bar{\beta}}{e^{\bar{\alpha}\bar{\beta}} - 1} - 1 - \bar{\alpha}\bar{Q} \right), \\ \bar{F}_{L_2}(\bar{t}) &= \frac{\bar{K}\bar{\alpha}\bar{\beta}}{e^{\bar{\alpha}\bar{\beta}} - 1} \bar{w}_2(\bar{t}) + \bar{K}\bar{\alpha}\bar{\beta}\bar{\tau} \frac{1 - e^{\bar{\alpha}\bar{\beta}} + \bar{\alpha}\bar{\beta}e^{\bar{\alpha}\bar{\beta}}}{(e^{\bar{\alpha}\bar{\beta}} - 1)^2} \dot{w}_2(t) \\ &\quad + \bar{K} \left( \frac{\bar{\alpha}\bar{\beta}}{e^{\bar{\alpha}\bar{\beta}} - 1} - 1 - \bar{\alpha}\bar{Q} \right), \\ \bar{F}_{L_3}(\bar{t}) &= \frac{\bar{K}\bar{\alpha}\bar{\beta}}{e^{\bar{\alpha}\bar{\beta}} - 1} \bar{w}_3(\bar{t}) + \bar{K}\bar{\alpha}\bar{\beta}\bar{\tau} \frac{1 - e^{\bar{\alpha}\bar{\beta}} + \bar{\alpha}\bar{\beta}e^{\bar{\alpha}\bar{\beta}}}{(e^{\bar{\alpha}\bar{\beta}} - 1)^2} \dot{w}_3(t) \\ &\quad + \bar{K} \left( \frac{\bar{\alpha}\bar{\beta}}{e^{\bar{\alpha}\bar{\beta}} - 1} - 1 - \bar{\alpha}\bar{Q} \right). \end{aligned} \quad (14)$$

### C. Governing equations

By defining  $\bar{F}_d = F_d/mg$ ,  $\bar{a}_0 = \frac{a_0}{m} \sqrt{\frac{L}{g}}$ ,  $\bar{a}_1 = \frac{a_1 L}{m}$ , and combining with Eqs. (5) and (14), Eq. (3) can be expressed

as [72]

$$\begin{aligned}
& \ddot{w}_1(\bar{t}) - 1 - k[\lambda_2 \bar{L}_2 - \bar{L}_2 - 3\bar{w}_1(\bar{t}) - \bar{w}_2(\bar{t}) - \bar{w}_3(\bar{t})] + \frac{\bar{K} \bar{\alpha} \bar{\beta}}{e^{\bar{\alpha} \bar{\beta}} - 1} [\bar{w}_1(\bar{t}) + \lambda_1 - 1] \\
& + \bar{K} \bar{\alpha} \bar{\beta} \bar{\tau} \frac{1 - e^{\bar{\alpha} \bar{\beta}} + \bar{\alpha} \bar{\beta} e^{\bar{\alpha} \bar{\beta}}}{(e^{\bar{\alpha} \bar{\beta}} - 1)^2} \dot{w}_1(\bar{t}) + \bar{K} \left( \frac{\bar{\alpha} \bar{\beta}}{e^{\bar{\alpha} \bar{\beta}} - 1} - 1 - \bar{\alpha} \bar{Q} \right) + (\bar{a}_0 + \bar{a}_1 |\dot{w}_1(\bar{t})|) \dot{w}_1(\bar{t}) = 0, \\
& \ddot{w}_2(\bar{t}) - 1 - k[\lambda_2 \bar{L}_2 - \bar{L}_2 - 3\bar{w}_2(\bar{t}) - \bar{w}_1(\bar{t}) - \bar{w}_3(\bar{t})] + \frac{\bar{K} \bar{\alpha} \bar{\beta}}{e^{\bar{\alpha} \bar{\beta}} - 1} [\bar{w}_2(\bar{t}) + \lambda_1 - 1] \\
& + \bar{K} \bar{\alpha} \bar{\beta} \bar{\tau} \frac{1 - e^{\bar{\alpha} \bar{\beta}} + \bar{\alpha} \bar{\beta} e^{\bar{\alpha} \bar{\beta}}}{(e^{\bar{\alpha} \bar{\beta}} - 1)^2} \dot{w}_2(\bar{t}) + \bar{K} \left( \frac{\bar{\alpha} \bar{\beta}}{e^{\bar{\alpha} \bar{\beta}} - 1} - 1 - \bar{\alpha} \bar{Q} \right) + (\bar{a}_0 + \bar{a}_1 |\dot{w}_2(\bar{t})|) \dot{w}_2(\bar{t}) = 0, \\
& \ddot{w}_3(\bar{t}) - 1 - k[\lambda_2 \bar{L}_2 - \bar{L}_2 - 3\bar{w}_3(\bar{t}) - \bar{w}_1(\bar{t}) - \bar{w}_2(\bar{t})] + \frac{\bar{K} \bar{\alpha} \bar{\beta}}{e^{\bar{\alpha} \bar{\beta}} - 1} [\bar{w}_3(\bar{t}) + \lambda_1 - 1] \\
& + \bar{K} \bar{\alpha} \bar{\beta} \bar{\tau} \frac{1 - e^{\bar{\alpha} \bar{\beta}} + \bar{\alpha} \bar{\beta} e^{\bar{\alpha} \bar{\beta}}}{(e^{\bar{\alpha} \bar{\beta}} - 1)^2} \dot{w}_3(\bar{t}) + \bar{K} \left( \frac{\bar{\alpha} \bar{\beta}}{e^{\bar{\alpha} \bar{\beta}} - 1} - 1 - \bar{\alpha} \bar{Q} \right) + (\bar{a}_0 + \bar{a}_1 |\dot{w}_3(\bar{t})|) \dot{w}_3(\bar{t}) = 0. \tag{15}
\end{aligned}$$

Equation (15) represents a second-order differential equation with variable coefficients. In this research, the classical fourth-order Runge-Kutta method is adopted to numerically solve Eq. (15) by using the MATLAB software. This approach allows us to obtain the steady-state response of the LCE fiber, which obtains the displacement and velocity of self-oscillation over time.

### III. TWO MOTION REGIMES AND THE MECHANISM

In this section, three synchronous modes, namely, full synchronous mode, partial synchronous mode, and asynchronous mode, are described first. Then, two motion regimes, namely, static and self-oscillation regimes, are found, and the mechanism of self-oscillation is revealed in detail.

To further investigate the coupled self-oscillating synchronous system, it is imperative to obtain standard values for dimensionless system parameters. Based on previous experiments and data [72–77], Table I lists the actual values of the system parameters, while corresponding dimensionless parameters are computed and presented in Table II.

TABLE I. Properties of the material and geometric parameters.

Parameter	Definition	Value	Unit
$L$	Original length of LCE fiber	0.01–1	m
$m$	Mass	0.01–0.1	kg
$g$	Acceleration of gravity	9.8	m/s <sup>2</sup>
$\rho_c$	Heat capacity	0.02–0.5	J/m <sup>2</sup> /C
$h$	Heat transfer coefficient	1–20	W/m <sup>2</sup> /C
$K$	LCE elastic coefficient	10–100	N/m
$k$	Spring elastic coefficient	10–100	N/m
$\alpha$	Thermal expansion coefficient	–0.4–0	1/C
$\beta$	Temperature gradient	20–1000	C/m
$a_0$	First damping coefficient	0–0.5	kg/s
$a_1$	Second damping coefficient	0–1	kg/s
$\tau$	Characteristic time	0.001–0.5	s

#### A. Three synchronization modes and two motion regimes

A time history curve of each mass can be obtained by numerical calculation, with setting appropriate system parameters  $\bar{K}$ ,  $\bar{k}$ ,  $\bar{\alpha}$ ,  $\bar{\beta}$ ,  $\bar{a}_0$ ,  $\bar{a}_1$ ,  $\bar{\tau}$ ,  $v_1^0$ ,  $v_2^0$ , and  $v_3^0$ . Figure 2 shows that there are three synchronous modes, namely, fully synchronous mode, partial synchronous mode, and asynchronous mode. In calculations, the dimensionless parameters are selected as  $\bar{K} = 14$ ,  $\bar{k} = 6$ ,  $\bar{\alpha} = -0.2$ ,  $\bar{\beta} = 0.6$ ,  $\bar{a}_1 = 0.6$ , and  $\bar{\tau} = 0.15$ . When  $\bar{a}_0 = 0.2$ , the three LCE fibers with same velocities, initially oscillate under a linear temperature field. Subsequently, due to the damping force, the amplitude gradually decreases until it becomes stationary, as illustrated in Figs. 2(a), 2(c), and 2(e). This is because the energy absorbed by the fiber when heated cannot compensate for the damping dissipation. Conversely, when  $\bar{a}_0 = 0.02$ , the LCE fiber can oscillate periodically and constantly in the temperature field, namely, the self-oscillation regime, as plotted in Figs. 2(b), 2(d), and 2(f). This is because the net work done by the tension of the LCE fiber can compensate for the damping dissipation. Furthermore, the system has three synchronous modes, and when  $v_1^0 = 0$ ,  $v_2^0 = 0$ , and  $v_3^0 = 0$ , the system reaches full synchronous mode, where the time history curves of the LCE fibers are exactly the same as shown in Fig. 2(b). It can be seen from Fig. 2(d) that when  $v_1^0 = 5$ ,  $v_2^0 = 0$ , and  $v_3^0 = 0$ , the system is the partial synchronous mode. And Fig. 2(e) shows that the system is asynchronous mode when  $v_1^0 = 1$ ,  $v_2^0 = 0$ , and  $v_3^0 = -5$ .

#### B. The mechanism of self-oscillation

To further study the mechanism of self-oscillation, Fig. 3 draws the changes of several key quantities in the process of self-oscillation, where the system parameters of the full

TABLE II. Dimensionless parameters.

Parameter	$\bar{K}$	$\bar{k}$	$\bar{\alpha}$	$\bar{\beta}$	$\bar{a}_0$	$\bar{a}_1$	$\bar{\tau}$
Value	1–20	2–15	–0.4–0	0–1	0–0.2	0–1	0.01–0.2

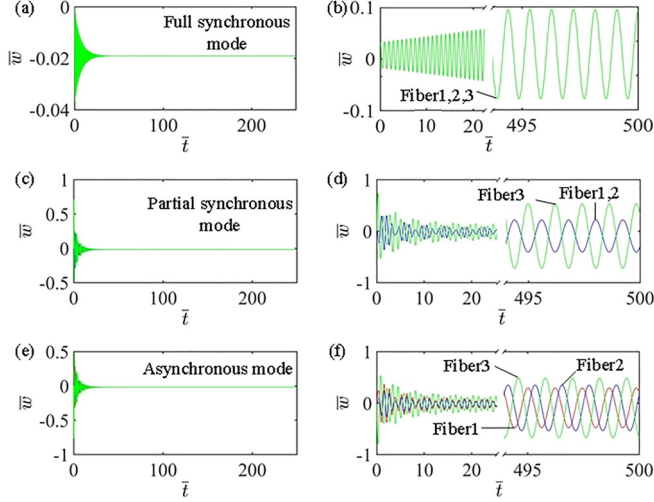


FIG. 2. Three synchronous modes and two motion regimes of the coupled self-oscillating system, where the parameters are  $\bar{K} = 14$ ,  $\bar{k} = 6$ ,  $\bar{\alpha} = -0.2$ ,  $\bar{\beta} = 0.6$ ,  $\bar{a}_0 = 0.6$ , and  $\bar{\tau} = 0.15$ . (a) Static regime in full synchronous mode, and the parameter is set as  $\bar{a}_0 = 0.2$ ,  $v_1^0 = 0$ ,  $v_2^0 = 0$ , and  $v_3^0 = 0$ . (b) Self-oscillation regime in full synchronous mode, and the parameters are set as  $\bar{a}_0 = 0.02$ ,  $v_1^0 = 0$ ,  $v_2^0 = 0$ , and  $v_3^0 = 0$ . (c) Static regime in partial synchronous mode, and the parameters are set as  $\bar{a}_0 = 0.2$ ,  $v_1^0 = 0$ ,  $v_2^0 = 0$ , and  $v_3^0 = 5$ . (d) Self-oscillation regime in partial synchronous mode, and the parameters are set as  $\bar{a}_0 = 0.02$ ,  $v_1^0 = 0$ ,  $v_2^0 = 0$ , and  $v_3^0 = 5$ . (e) Static regime in asynchronous mode, and the parameters are set as  $\bar{a}_0 = 0.2$ ,  $v_1^0 = 1$ ,  $v_2^0 = 0$ , and  $v_3^0 = -5$ . (f) Self-oscillation regime in asynchronous mode, and the parameters are set as  $\bar{a}_0 = 0.02$ ,  $v_1^0 = 1$ ,  $v_2^0 = 0$ , and  $v_3^0 = -5$ . There exist three synchronous modes of the system, that is, full synchronous mode, partial synchronous mode, and asynchronous mode.

synchronous mode are  $\bar{K} = 14$ ,  $\bar{k} = 6$ ,  $\bar{\alpha} = -0.2$ ,  $\bar{\beta} = 0.6$ ,  $\bar{a}_0 = 0.02$ ,  $\bar{a}_1 = 0.6$ ,  $\bar{\tau} = 0.15$ ,  $v_1^0 = 0$ ,  $v_2^0 = 0$ , and  $v_3^0 = 0$ . The parameters of the partial synchronous mode are set as  $\bar{K} = 14$ ,  $\bar{k} = 6$ ,  $\bar{\alpha} = -0.2$ ,  $\bar{\beta} = 0.6$ ,  $\bar{a}_0 = 0.02$ ,  $\bar{a}_1 = 0.6$ ,  $\bar{\tau} = 0.15$ ,  $v_1^0 = 5$ ,  $v_2^0 = 0$ , and  $v_3^0 = 0$ . The parameters of the asynchronous mode are set as  $\bar{K} = 14$ ,  $\bar{k} = 6$ ,  $\bar{\alpha} = -0.2$ ,  $\bar{\beta} = 0.6$ ,  $\bar{a}_0 = 0.02$ ,  $\bar{a}_1 = 0.6$ ,  $\bar{\tau} = 0.15$ ,  $v_1^0 = 1$ ,  $v_2^0 = 0$ , and  $v_3^0 = -5$ . Figures 3(a)–3(c) display the time history curves in the three synchronous modes, illustrating that the LCE fiber can oscillate periodically under linear temperature field. Figures 3(d)–3(f) plot the changes of the tension of the LCE fibers over time, explaining the periodic change of the driving force. Figures 3(g)–3(i) plot the damping force over time in the three synchronous modes, indicating that the damping force changes periodically over time. Figures 3(j)–3(l) show the relationship between the tension of LCE fibers and displacements, where the area of hysteresis loop enclosed indicates the net work. Figures 3(m)–3(o) illustrate the relationship between the damping force and displacement, where the area of hysteresis loop enclosed is the damping dissipation. By further calculation, the area of hysteresis loops in Figs. 3(j)–3(l) and 3(m)–3(o) are equal, which means that the net work done by the LCE fiber can compensate the damping dissipation, so the self-oscillation of the system can maintain.

#### IV. PARAMETER STUDY IN THE FULL SYNCHRONOUS MODE

In Eq. (15), there are seven dimensionless parameters:  $\bar{K}$ ,  $\bar{k}$ ,  $\bar{\alpha}$ ,  $\bar{\beta}$ ,  $\bar{a}_0$ ,  $\bar{a}_1$ , and  $\bar{\tau}$ , which can affect the self-oscillation. In this section, the effect of these seven parameters on the self-oscillation of the full synchronous mode is investigated in detail.

##### A. Effects of thermal expansion coefficient

Figure 4 plots how the thermal expansion coefficient  $\bar{\alpha}$  affects the system in the full synchronous mode, where other system parameters are selected as  $\bar{K} = 14$ ,  $\bar{k} = 6$ ,  $\bar{\beta} = 0.6$ ,  $\bar{a}_0 = 0.02$ ,  $\bar{a}_1 = 0.6$ ,  $\bar{\tau} = 0.15$ ,  $v_1^0 = 0$ ,  $v_2^0 = 0$ , and  $v_3^0 = 0$ . It can be seen from Fig. 4(a) that  $|\bar{\alpha}| = 0.05$  is a critical value between static and self-oscillation regimes. As shown in Fig. 4(a), when  $|\bar{\alpha}| < 0.05$ , the system is in the static regime. On the contrary, when  $|\bar{\alpha}| > 0.05$ , the amplitude of the system increases with the increase of the absolute value of the thermal expansion coefficient, while the frequency is not affected. This is because with the increase of the absolute value of  $\bar{\alpha}$ , the contraction of the LCE fiber increases, the driving force of the system increases, and thus the amplitude increases. Figure 4(b) plots three limit cycles for different thermal expansion coefficients  $\bar{\alpha}$ .

Further calculations show that the system exhibits a full synchronous mode when the thermal expansion coefficients of the three LCE fibers are identical, as depicted in Fig. 5(a). In the case where the thermal expansion coefficients of LCE fibers 1, 2, and 3 are  $-0.3$ ,  $-0.2$ , and  $-0.2$ , respectively, the system operates in the partial synchronous mode, as illustrated in Fig. 5(b). Furthermore, when the thermal expansion coefficients of LCE fibers 1, 2, and 3 are  $-0.3$ ,  $-0.2$ , and  $-0.1$ , respectively, the system transits into asynchronous mode, as shown in Fig. 5(c). Other system parameters, such as elastic coefficient and spring coefficient, have the potential to influence the self-oscillation synchronization mode. In this study, we focus on the synchronization phenomenon in three coupled identical self-oscillators. In the following parametric analysis, the system parameters for the three coupled self-oscillators are set to be identical. A detailed quantitative analysis of synchronization behaviors among nonidentical coupled self-oscillators could serve as a subject for future work.

##### B. Effects of LCE elastic coefficient

Figure 6 draws how the LCE elastic coefficient affects the system in the full synchronous mode, where other system parameters are  $\bar{k} = 6$ ,  $\bar{\alpha} = -0.2$ ,  $\bar{\beta} = 0.6$ ,  $\bar{a}_0 = 0.02$ ,  $\bar{a}_1 = 0.6$ ,  $\bar{\tau} = 0.15$ ,  $v_1^0 = 0$ ,  $v_2^0 = 0$ , and  $v_3^0 = 0$ . Figure 6(a) shows that there is a critical  $\bar{K} = 3$  between static and self-oscillation regimes. When  $\bar{K} < 3$ , the system is in the static regime, while when  $\bar{K} > 3$ , the system is in the self-oscillation regime; there are increases in both amplitude and frequency as  $\bar{K}$  increases. This is because with the increase of  $\bar{K}$ , the tension  $F_L$  of the LCE fibers increases, namely, the driving force increases, so the amplitude and frequency increase. Figure 6(b) illustrates the limit cycles with different  $\bar{K}$  in the full synchronous mode.

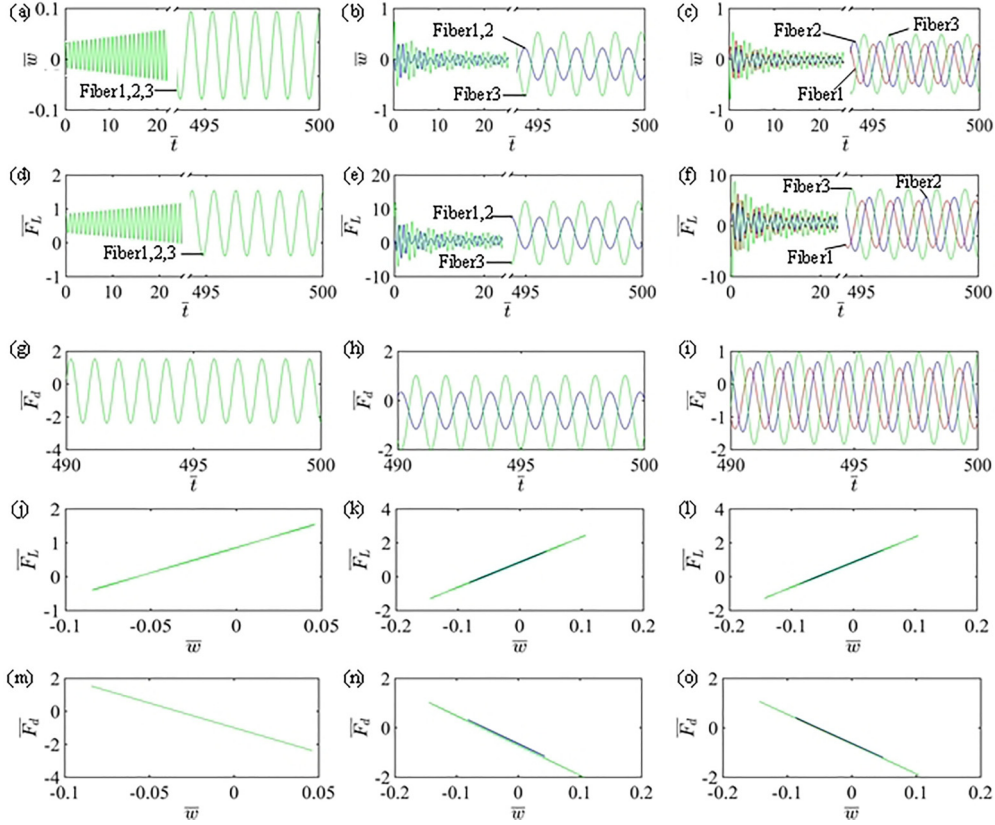


FIG. 3. Mechanism of the self-oscillation. The parameters of the full synchronous mode are set as  $\bar{K} = 14$ ,  $\bar{k} = 6$ ,  $\bar{\alpha} = -0.2$ ,  $\bar{\beta} = 0.6$ ,  $\bar{a}_0 = 0.02$ ,  $\bar{a}_1 = 0.6$ ,  $\bar{\tau} = 0.15$ ,  $v_1^0 = 0$ ,  $v_2^0 = 0$ , and  $v_3^0 = 0$ . The parameters of the partial synchronous mode are set as  $\bar{K} = 14$ ,  $\bar{k} = 6$ ,  $\bar{\alpha} = -0.2$ ,  $\bar{\beta} = 0.6$ ,  $\bar{a}_0 = 0.02$ ,  $\bar{a}_1 = 0.6$ ,  $\bar{\tau} = 0.15$ ,  $v_1^0 = 5$ ,  $v_2^0 = 0$ , and  $v_3^0 = 0$ . The parameters of the asynchronous mode are set as  $\bar{K} = 14$ ,  $\bar{k} = 6$ ,  $\bar{\alpha} = -0.2$ ,  $\bar{\beta} = 0.6$ ,  $\bar{a}_0 = 0.02$ ,  $\bar{a}_1 = 0.6$ ,  $\bar{\tau} = 0.15$ ,  $v_1^0 = 1$ ,  $v_2^0 = 0$ , and  $v_3^0 = -5$ . (a)–(c) Time history curve of full synchronous mode, partial synchronous mode, and asynchronous mode. (d)–(f) Curves of the tension of LCE fiber change over time in the full synchronous mode, partial synchronous mode, and asynchronous mode. (g)–(i) Curves of damping forces change with time in full synchronous mode, partial synchronous mode, and asynchronous mode. (j)–(l) The relationship between displacement and the tension of LCE fibers in full synchronous mode, partial synchronous mode, and asynchronous mode. (m)–(o) The relationship between displacement and the damping forces in full synchronous mode, partial synchronous mode, and asynchronous mode. The energy absorbed by the fibers from the temperature field can offset damping dissipation, enabling the system to sustain self-oscillation.

### C. Effects of spring elastic coefficient

Figure 7(a) plots the effect of spring elastic coefficient  $k$  on the amplitude and frequency in the full synchronous mode, where other system parameters are selected as  $\bar{k} = 6$ ,  $\bar{\alpha} = -0.2$ ,  $\bar{\beta} = 0.6$ ,  $\bar{a}_0 = 0.02$ ,  $\bar{a}_1 = 0.6$ ,  $\bar{\tau} = 0.15$ ,  $v_1^0 = 0$ ,  $v_2^0 = 0$ , and  $v_3^0 = 0$ . As shown in Fig. 7(a), the amplitude

decreases with the increase of  $k$ , and the frequency increases with the increase of  $k$ . This is because with the increase of the spring elastic coefficient, the recovery force of the system increases, which inhibits the system self-oscillation, thus the amplitude decreases. Figure 7(b) draws three limit cycles with different  $k$  in the full synchronous mode. The results show that the system is always in the self-oscillation regime of the full synchronous mode as the spring elastic coefficient changes.

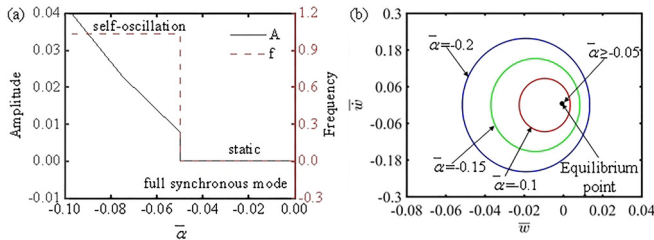


FIG. 4. The effect of the thermal expansion coefficient on the self-oscillation in full synchronous mode. (a) Variations of amplitude and frequency with different thermal expansion coefficients. (b) Limit cycles with  $\bar{\alpha} = -0.1$ ,  $\bar{\alpha} = -0.15$ , and  $\bar{\alpha} = -0.2$ .

### D. Effects of temperature gradient

Figure 8 shows how the temperature gradient affects the system in full synchronous mode, where other system parameters are chosen as  $\bar{K} = 14$ ,  $\bar{k} = 6$ ,  $\bar{\alpha} = -0.2$ ,  $\bar{a}_0 = 0.02$ ,  $\bar{a}_1 = 0.6$ ,  $\bar{\tau} = 0.15$ ,  $v_1^0 = 0$ ,  $v_2^0 = 0$ , and  $v_3^0 = 0$ . In Fig. 8(a),  $\bar{\beta} = 0.2$  is a critical value between two motion regimes, where with  $\bar{\beta} < 0.2$  the system is in static regime, while the system is in self-oscillation regime with  $\bar{\beta} > 0.2$ . Meanwhile, the amplitude of the system increases with an increase of  $\bar{\beta}$ , while the frequency is unchanged. The reason is, as  $\bar{\beta}$  increases, the temperature increases faster, and the LCE fiber is able

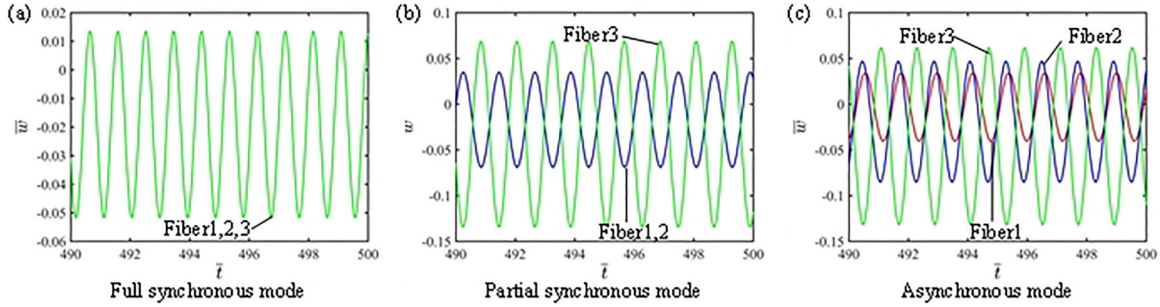


FIG. 5. Synchronization modes of three coupled nonidentical self-oscillators with different thermal expansion coefficients. (a) Full synchronous mode. (b) Partial synchronous mode. (c) Asynchronous mode.

to absorb more heat energy, which is converted into more kinetic energy, so the amplitude increases. In Fig. 8(b), the limit cycles of different  $\beta$  for full synchronous modes are plotted.

**E. Effects of the first damping coefficient**

Figure 9 shows how the first damping coefficient  $\bar{a}_0$  affects the system in the full synchronous mode, where other system parameters are selected as  $\bar{K} = 14$ ,  $\bar{k} = 6$ ,  $\bar{\alpha} = -0.2$ ,  $\bar{\beta} = 0.6$ ,  $\bar{a}_1 = 0.6$ ,  $\bar{\tau} = 0.15$ ,  $v_1^0 = 0$ ,  $v_2^0 = 0$ ,  $v_3^0 = 0$ .  $\bar{a}_0 = 0.12$  is a critical value between two motion regimes as shown in Fig. 9, where the system is in the static regime as  $\bar{a}_0 > 0.12$  and the system is in the self-oscillation regime with  $\bar{a}_0 < 0.12$ . Further, the amplitude decreases with increasing  $\bar{a}_0$ , while frequency is not affected. This is because when the first damping coefficient increases, the damping dissipation increases, and then the system kinetic energy decreases, thus the amplitude decreases. Figure 9(b) draws three limit cycles for different  $\bar{a}_0$  in the full synchronous mode.

**F. Effects of the second damping coefficient**

Figure 10 shows how the second damping coefficient  $\bar{a}_1$  affects the system in full synchronous mode, where other system parameters are selected as  $\bar{K} = 14$ ,  $\bar{k} = 6$ ,  $\bar{\alpha} = -0.2$ ,  $\bar{\beta} = 0.6$ ,  $\bar{a}_0 = 0.02$ ,  $\bar{\tau} = 0.15$ ,  $v_1^0 = 0$ ,  $v_2^0 = 0$ , and  $v_3^0 = 0$ . Figure 10(a) shows that the second damping coefficient does not affect the motion regimes of the system. In Fig. 10(a), the amplitude decreases with the increase of  $\bar{a}_1$ , while the frequency remains unchanged. This is because when the first damping coefficient increases, it leads to higher damping dissipation, resulting in a reduction in the system's kinetic

energy, so the amplitude decreases. Figure 10(b) plots three limit cycles for different  $\bar{a}_1$  in the full synchronous mode.

**G. Effects of characteristic time**

Figure 11 shows the effect of characteristic time  $\bar{\tau}$  on the system in full synchronous mode, where other parameters are  $\bar{K} = 14$ ,  $\bar{k} = 6$ ,  $\bar{\alpha} = -0.2$ ,  $\bar{\beta} = 0.6$ ,  $\bar{a}_0 = 0.02$ ,  $\bar{a}_1 = 0.6$ ,  $v_1^0 = 0$ ,  $v_2^0 = 0$ , and  $v_3^0 = 0$ . It can be concluded from Fig. 11(a) that  $\bar{\tau} = 0.03$  is a critical characteristic time between two motion regimes. As shown in Fig. 11(a), the system reaches the static regime for  $\bar{\tau} < 0.03$ , while the system is the self-oscillation regime for  $\bar{\tau} > 0.03$ . Meanwhile, the amplitude increases with an increase of  $\bar{\tau}$ , while the frequency remains unchanged. This is because with the increase of the characteristic time, the heat transfer rate increases, leading the LCE fiber to absorb more heat energy, the tension of the LCE fiber can do more work, and the amplitude increases. Figure 11(b) draws three limit cycles with different  $\bar{\tau}$  in the full synchronous mode.

**V. PARAMETER STUDY IN THE PARTIAL SYNCHRONOUS MODE**

In this section, the effect of system parameters on self-oscillation in the partial synchronous mode is investigated in detail. For ease of description, the amplitude and frequency of LCE fiber 1 and LCE fiber 2 are written as  $A_{1,2}$  and  $f_{1,2}$ . The amplitude and frequency of LCE fiber 3 are written as  $A_3$  and  $f_3$ .

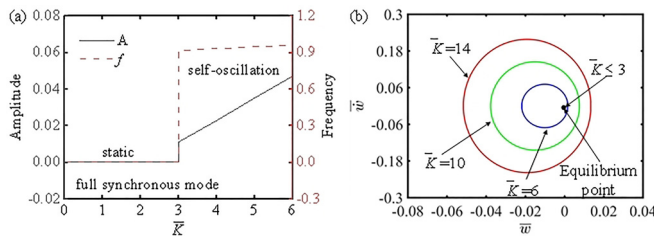


FIG. 6. The effect of an LCE elastic coefficient on the self-oscillation in full synchronous mode. (a) Variations of amplitude and frequency with different LCE elastic coefficients. (b) Limit cycles with  $\bar{K} = 14$ ,  $\bar{K} = 10$ , and  $\bar{K} = 6$ .

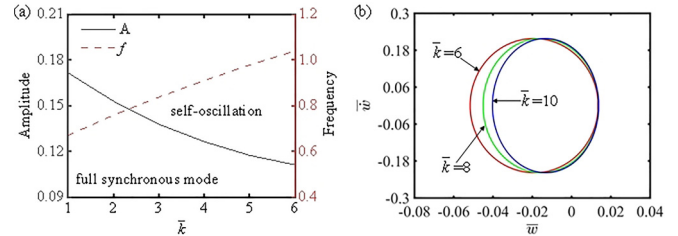


FIG. 7. The effect of spring elastic coefficient on the self-oscillation in full synchronous mode. (a) Variations of amplitude and frequency with different spring elastic coefficients. (b) Limit cycles with  $\bar{k} = 6$ , and  $\bar{k} = 10$ .

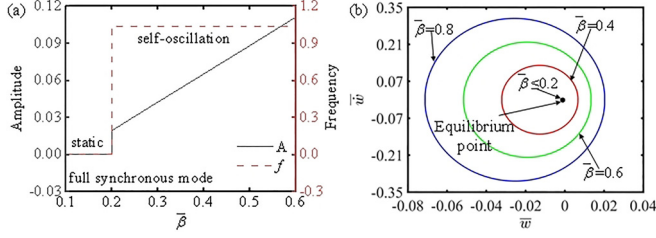


FIG. 8. The effect of temperature gradient on the self-oscillation in full synchronous mode. (a) Variations of amplitude and frequency with different temperature gradient. (b) Limit cycles with  $\bar{\beta} = 0.4$ ,  $\bar{\beta} = 0.6$ , and  $\bar{\beta} = 0.8$ .

### A. Effects of thermal expansion coefficient

Figure 12 draws how the thermal expansion coefficient  $\bar{\alpha}$  affects the system in the partial synchronous mode, where other system parameters are selected as  $\bar{K} = 14$ ,  $\bar{k} = 6$ ,  $\bar{\beta} = 0.6$ ,  $\bar{a}_0 = 0.02$ ,  $\bar{a}_1 = 0.6$ ,  $\bar{\tau} = 0.15$ ,  $v_1^0 = 0$ ,  $v_2^0 = 0$ , and  $v_3^0 = 5$ . As shown in Fig. 12(a),  $|\bar{\alpha}| = 0.05$  is a critical thermal expansion coefficient between two motion regimes. When  $|\bar{\alpha}| < 0.05$ , the system is in the static regime, while the system is in the self-oscillation regime with  $|\bar{\alpha}| > 0.05$ , and the amplitude  $A_{1,2}$  is less than  $A_3$  and  $f_{1,2}$  is consistent with  $f_3$ . Figure 12(a) illustrates that the amplitude and frequency decrease as  $\bar{\alpha}$  increases. This is because the greater the thermal expansion coefficient, the greater the amount of LCE fiber thermal drive contraction, the greater the tension of the LCE fiber, the greater the driving force of the system, and thus the greater the amplitude. Figure 12(b) draws three limit cycles for different  $\bar{\alpha}$  in the partial synchronous mode.

### B. Effects of LCE elastic coefficient

Figure 13 draws how the LCE elastic coefficient affects the system in the partial synchronous mode, where other system parameters are  $\bar{k} = 6$ ,  $\bar{\alpha} = -0.2$ ,  $\bar{\beta} = 0.6$ ,  $\bar{a}_0 = 0.02$ ,  $\bar{a}_1 = 0.6$ ,  $\bar{\tau} = 0.15$ ,  $v_1^0 = 0$ ,  $v_2^0 = 0$ , and  $v_3^0 = 5$ . As shown in Fig. 13(a), there is a critical value  $\bar{K} = 3$  between two regimes. The system is in the static regime, with  $\bar{K} < 3$ , and the system is in self-oscillation regime with  $\bar{K} > 3$ , and the amplitude  $A_{1,2}$  is less than  $A_3$  and  $f_{1,2}$  is consistent with  $f_3$ . Figure 13(a) shows that amplitude and frequency increase as  $\bar{K}$  increases. This is because the greater the LCE elastic coefficient, the greater the tension of the LCE fiber when it contracts, the greater the driving force of the system, and

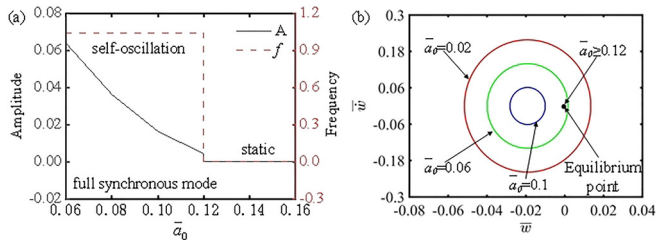


FIG. 9. The effect of the first damping coefficient on the self-oscillation in full synchronous mode. (a) Variations of amplitude and frequency with different first damping coefficients. (b) Limit cycles with  $\bar{a}_0 = 0.02$ ,  $\bar{a}_0 = 0.06$ , and  $\bar{a}_0 = 0.1$ .

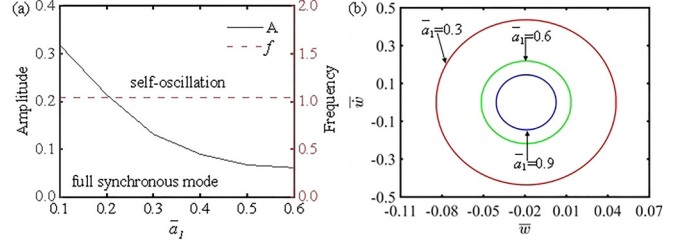


FIG. 10. The effect of the second damping coefficient on the self-oscillation in full synchronous mode. (a) Variations of amplitude and frequency with different second damping coefficients. (b) Limit cycles with  $\bar{a}_1 = 0.3$ ,  $\bar{a}_1 = 0.6$ , and  $\bar{a}_1 = 0.9$ .

thus the greater the amplitude. Figure 13(b) draws three limit cycles for different  $\bar{K}$  in the partial synchronous mode.

### C. Effects of spring elastic coefficient

Figure 14 shows how the spring elastic coefficient  $\bar{k}$  affects the system in the partial synchronous mode, where other system parameters are selected as  $\bar{k} = 6$ ,  $\bar{\alpha} = -0.2$ ,  $\bar{\beta} = 0.6$ ,  $\bar{a}_0 = 0.02$ ,  $\bar{a}_1 = 0.6$ ,  $\bar{\tau} = 0.15$ ,  $v_1^0 = 0$ ,  $v_2^0 = 0$ , and  $v_3^0 = 5$ . As shown in Fig. 14(a), the system is always in the self-oscillation regime as  $\bar{k}$  increases. It can be seen from Fig. 14(a) that  $A_{1,2}$  is less than  $A_3$ , and  $f_{1,2}$  is the same as  $f_3$ . It can be seen from Fig. 14(a) that the amplitude decreases as  $\bar{k}$  increases, while the frequency increases as  $\bar{k}$  increases. This is because with the increase of the spring elastic coefficient, the recovery force of the system increases, which inhibits the self-oscillation, thus the amplitude decreases. Figure 14(b) draws three limit cycles with different  $\bar{k}$  in the partial synchronous mode.

### D. Effects of temperature gradient

Figure 15 shows how the temperature gradient affects the system in the partial synchronous mode, where other system parameters are chosen as  $\bar{K} = 14$ ,  $\bar{k} = 6$ ,  $\bar{\alpha} = -0.2$ ,  $\bar{a}_0 = 0.02$ ,  $\bar{a}_1 = 0.6$ ,  $\bar{\tau} = 0.15$ ,  $v_1^0 = 0$ ,  $v_2^0 = 0$ , and  $v_3^0 = 5$ . Figure 15(a) shows that  $\bar{\beta} = 0.08$  is a critical temperature gradient between the static and self-oscillation regimes. When  $\bar{\beta} < 0.08$ , the system is in the static regime, and the system is in the self-oscillation regime when  $\bar{\beta} > 0.08$ . Meanwhile, the amplitudes of LCE fiber 1 and LCE fiber 2 are smaller than LCE fiber 3. In addition, the amplitude increases with

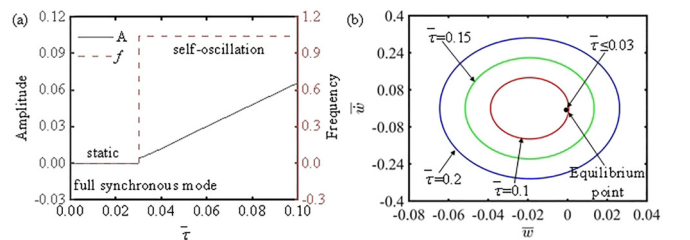


FIG. 11. The effect of characteristic time on the self-oscillation in full synchronous mode. (a) Variations of amplitude and frequency with characteristic time. (b) Limit cycles with  $\bar{\tau} = 0.1$ ,  $\bar{\tau} = 0.15$ , and  $\bar{\tau} = 0.2$ .

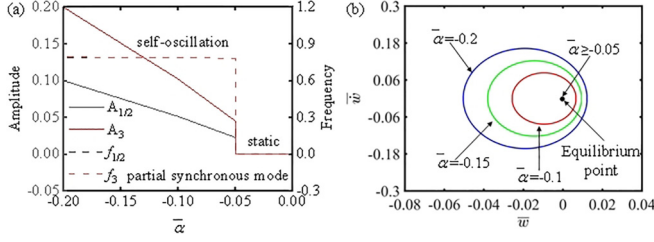


FIG. 12. The effect of coefficient of thermal expansion on the self-oscillation in partial synchronous mode. (a) Variations of amplitude and frequency with different coefficients of thermal expansion. (b) Limit cycles with  $\bar{\alpha} = -0.1$ ,  $\bar{\alpha} = -0.15$ , and  $\bar{\alpha} = -0.2$ .

the increase of temperature gradient, while the frequency remains constant. This is because as the temperature gradient increases, the temperature becomes higher, the amount of LCE fiber contraction increases, and the tension of the LCE fiber as the driving force increases, thus the amplitude increases. Three limit cycles of different temperature gradient in the partial synchronous mode are plotted in Fig. 15(b).

#### E. Effects of the first damping coefficient

Figure 16 shows how the the first damping coefficient  $\bar{a}_0$  affects the system in the partial synchronous mode, where other system parameters are selected as  $\bar{K} = 14$ ,  $\bar{k} = 6$ ,  $\bar{\alpha} = -0.2$ ,  $\bar{\beta} = 0.6$ ,  $\bar{a}_1 = 0.6$ ,  $\bar{\tau} = 0.15$ ,  $v_1^0 = 0$ ,  $v_2^0 = 0$ , and  $v_3^0 = 5$ . Figure 16(a) shows that  $\bar{a}_0 = 0.12$  is a critical first damping coefficient between two motion regimes. The system is in the static regime with  $\bar{a}_0 > 0.12$ , while the system is in the self-oscillation regime with  $\bar{a}_0 < 0.12$ . In addition, the amplitudes of LCE fiber 1 and LCE fiber 2 are smaller than that of LCE fiber 3. As shown in Fig. 16(a), the amplitude decreases with the increase of the first damping coefficient, while the frequency is basically unchanged. This is because the larger the first damping coefficient is, the damping dissipation increases, the kinetic energy of the system decreases, and thus the amplitude decreases. Figure 16(b) draws three limit cycles with different first damping coefficients of the partial synchronous mode.

#### F. Effects of the second damping coefficient

Figure 17 illustrates how the second damping coefficient  $\bar{a}_1$  affects the system in the partial synchronous mode, where

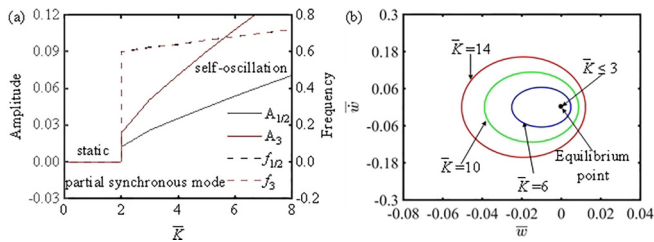


FIG. 13. The effect of LCE elastic coefficient on the self-oscillation in partial synchronous mode. (a) Variations of amplitude and frequency with different LCE elastic coefficients. (b) Limit cycles with  $\bar{K} = 14$ ,  $\bar{K} = 10$ , and  $\bar{K} = 6$ .

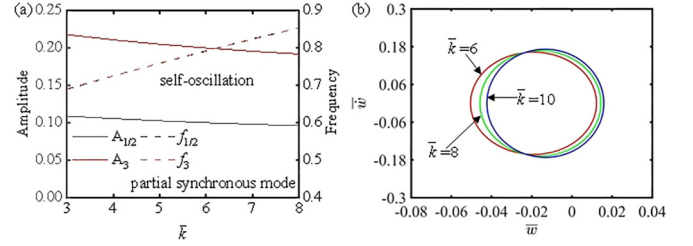


FIG. 14. The effect of spring elastic coefficient on the self-oscillation in partial synchronous mode. (a) Variations of amplitude and frequency with different spring elastic coefficients. (b) Limit cycles with  $\bar{k} = 6$ ,  $\bar{k} = 8$ , and  $\bar{k} = 10$ .

other system parameters are selected as  $\bar{K} = 14$ ,  $\bar{k} = 6$ ,  $\bar{\alpha} = -0.2$ ,  $\bar{\beta} = 0.6$ ,  $\bar{a}_0 = 0.02$ ,  $\bar{\tau} = 0.15$ ,  $v_1^0 = 0$ ,  $v_2^0 = 0$ , and  $v_3^0 = 5$ . Figure 17(a) shows that the system stays in the self-oscillation regime and the amplitudes of LCE fiber 1 and LCE fiber 2 are less than those of LCE fiber 3. Figure 17(a) also shows that the amplitude of self-oscillation decreases with increases of the second damping coefficient, while the frequency remains constant. This phenomenon can be attributed to the heightened damping dissipation associated with the larger values of the first damping coefficient, which leads to a reduction in the system's kinetic energy and, consequently, a decrease in amplitude. Figure 17(b) illustrates three limit cycles with different second damping coefficients of the partial synchronous mode.

#### G. Effects of characteristic time

Figure 18 shows how the characteristic time affects the system in the partial synchronous mode, where other system parameters are selected as  $\bar{K} = 14$ ,  $\bar{k} = 6$ ,  $\bar{\alpha} = -0.2$ ,  $\bar{\beta} = 0.6$ ,  $\bar{a}_0 = 0.02$ ,  $\bar{a}_1 = 0.6$ ,  $v_1^0 = 0$ ,  $v_2^0 = 0$ , and  $v_3^0 = 5$ . Figure 18(a) shows that  $\bar{\tau} = 0.02$  is a critical characteristic time between the static and self-oscillation regimes. The system is in the static regime with  $\bar{\tau} < 0.02$ , and the system is in the self-oscillation regime with  $\bar{\tau} > 0.02$ . Meanwhile, the amplitudes of LCE fiber 1 and LCE fiber 2 are smaller than those of LCE fiber 3. As shown in Fig. 18(a), the amplitude increases as the characteristic time increases, while the frequency remains constant. The reason for this is, with the increase of characteristic time, the heat transfer rate increases, leading the fiber to absorb more heat energy, the tension of LCE fiber can do more work, and the amplitude increases.

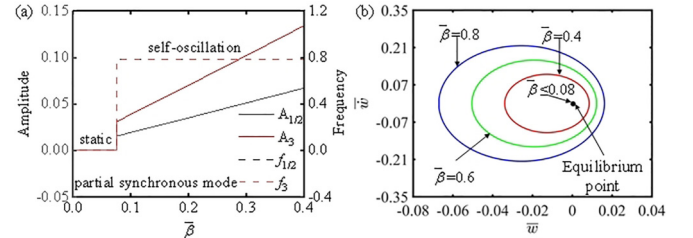


FIG. 15. The effect of temperature gradient on the self-oscillation in partial synchronous mode. (a) Variations of amplitude and frequency with different temperature gradients. (b) Limit cycles with  $\bar{\beta} = 0.4$ ,  $\bar{\beta} = 0.6$ , and  $\bar{\beta} = 0.8$ .

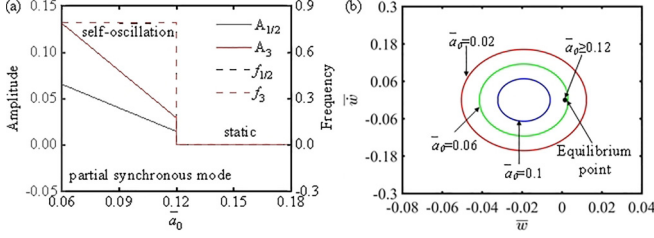


FIG. 16. The effect of the first damping coefficient on the self-oscillation in partial synchronous mode. (a) Variations of amplitude and frequency with different first damping coefficients. (b) Limit cycles with  $\bar{a}_0 = 0.02$ ,  $\bar{a}_0 = 0.06$ , and  $\bar{a}_0 = 0.1$ .

Figure 18(b) draws three limit cycles of different characteristic times of the partial synchronous mode.

## VI. PARAMETER STUDY IN THE ASYNCHRONOUS MODE

In this section, the effect of system parameters on self-oscillation in the asynchronous mode is investigated in detail. For ease of description, the amplitudes of the three LCE fibers are written as  $A_1$ ,  $A_2$ , and  $A_3$  and the frequencies of the three LCE fibers are written as  $f_1$ ,  $f_2$ , and  $f_3$ . The phase difference between LCE fiber 1 and LCE fiber 2 is written as  $\text{Pd}_{1,2}$ , and the phase difference between LCE fiber 2 and LCE fiber 3 is written as  $\text{Pd}_{2,3}$ .

### A. Effects of thermal expansion coefficient

In Fig. 19, the effects of the thermal expansion coefficient on the amplitude, frequency, and phase difference of the system in the asynchronous mode are depicted, where other system parameters are selected as  $\bar{K} = 14$ ,  $\bar{k} = 6$ ,  $\bar{\beta} = 0.6$ ,  $\bar{a}_0 = 0.02$ ,  $\bar{a}_1 = 0.6$ ,  $\bar{\tau} = 0.15$ ,  $v_1^0 = 1$ ,  $v_2^0 = 0$ , and  $v_3^0 = -5$ . Figure 19(a) shows that the system is in the static regime with  $|\bar{\alpha}| < 0.075$ , while the system is in the self-oscillation regime with  $|\bar{\alpha}| > 0.075$ . Figure 19(a) shows that an increase in the thermal expansion coefficient can lead to a decrease in the amplitude and frequency. The reason is, the greater  $|\bar{\alpha}|$  leads to a greater contraction of the LCE fiber, then the greater the LCE fiber tension, and thus the greater the amplitude. Figure 19(b) shows that when  $|\bar{\alpha}|$  is small, the system is in the asynchronous mode and the phase difference  $\text{Pd}_{1,2}$  is at its minimum, while the phase difference  $\text{Pd}_{2,3}$  is at its maximum.

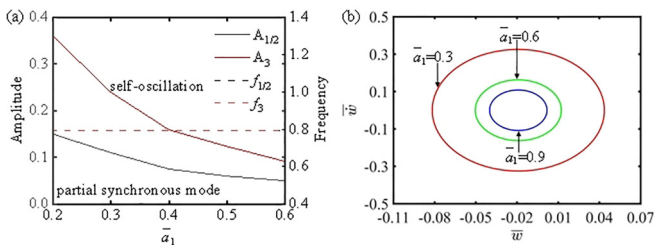


FIG. 17. The effect of the second damping coefficient on the self-oscillation in partial synchronous mode. (a) Variations of amplitude and frequency with different second damping coefficients. (b) Limit cycles with  $\bar{a}_1 = 0.3$ ,  $\bar{a}_1 = 0.6$ , and  $\bar{a}_1 = 0.9$ .

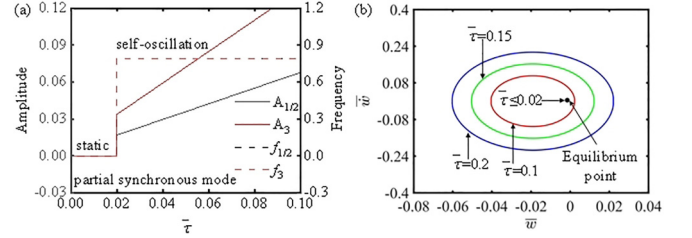


FIG. 18. The effect of characteristic time on the self-oscillation in partial synchronous mode. (a) Variations of amplitude and frequency with characteristic time. (b) Limit cycles with  $\bar{\tau} = 0.1$ ,  $\bar{\tau} = 0.15$ , and  $\bar{\tau} = 0.2$ .

As  $|\bar{\alpha}|$  increases, phase difference  $\text{Pd}_{1,2}$  gradually increases, while phase difference  $\text{Pd}_{2,3}$  decreases.

### B. Effects of LCE elastic coefficient

In Fig. 20, the influence of the LCE elastic coefficient on the amplitude, frequency, and phase difference of the system in the asynchronous mode is depicted, where other system parameters are  $\bar{k} = 6$ ,  $\bar{\alpha} = -0.2$ ,  $\bar{\beta} = 0.6$ ,  $\bar{a}_0 = 0.02$ ,  $\bar{a}_1 = 0.6$ ,  $\bar{\tau} = 0.15$ ,  $v_1^0 = 1$ ,  $v_2^0 = 0$ , and  $v_3^0 = -5$ . Figure 20(a) shows that the system is in the static regime with  $\bar{K} < 2$ , and the system is in the self-oscillation regime with  $\bar{K} > 2$ . Meanwhile, the amplitude and frequency increase as  $\bar{K}$  increases. The reason is, the greater the LCE elastic coefficient, the greater the elastic force, the greater the driving force, and thus the greater the amplitude. Figure 20(b) plots the phase difference between LCE fibers 1,2 and LCE fibers 2,3. As can be seen from Fig. 20(b), the phase difference  $\text{Pd}_{1,2}$  reaches its minimum, and the phase difference  $\text{Pd}_{2,3}$  reaches its maximum. Then the phase difference  $\text{Pd}_{1,2}$  increases with the increase of the LCE elastic coefficient, while the phase difference  $\text{Pd}_{2,3}$  decreases with the increase of the LCE elastic coefficient.

### C. Effects of spring elastic coefficient

Figure 21 illustrates how variations in the spring elastic coefficient impact the system's amplitude, frequency, and phase difference in the asynchronous mode, where other system parameters are selected as  $\bar{k} = 6$ ,  $\bar{\alpha} = -0.2$ ,  $\bar{\beta} = 0.6$ ,  $\bar{a}_0 = 0.02$ ,  $\bar{a}_1 = 0.6$ ,  $\bar{\tau} = 0.15$ ,  $v_1^0 = 1$ ,  $v_2^0 = 0$ , and  $v_3^0 = -5$ . Figure 21(a) reveals that the system is always in the self-

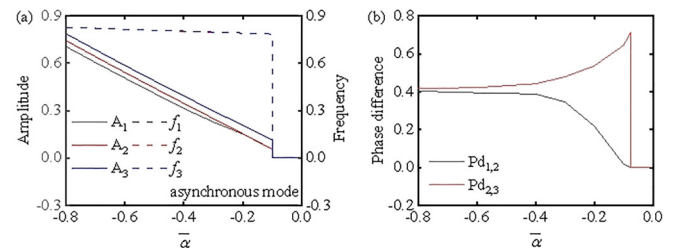


FIG. 19. The effect of thermal expansion coefficient on the self-oscillation in asynchronous mode. (a) Variations of amplitude and frequency with different thermal expansion coefficients. (b) Variations of phase difference with different thermal expansion coefficients.

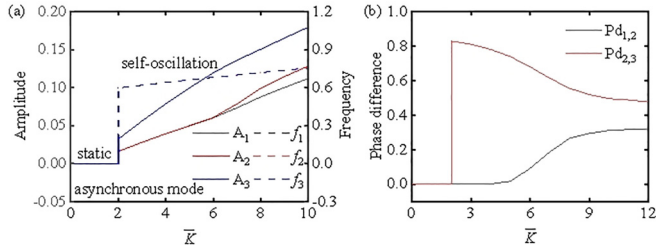


FIG. 20. The effect of LCE elastic coefficient on the self-oscillation in asynchronous mode. (a) Variations of amplitude and frequency with different LCE elastic coefficients. (b) Variations of phase difference with different LCE elastic coefficients.

oscillation regime, leading to a decrease in amplitude of self-oscillation and an increase in frequency as the spring elastic coefficient  $\bar{k}$  increases. This is because as the spring elastic coefficient increases, the recovery force of the system during oscillation increases, which inhibits the self-oscillation, and thus the amplitude decreases. It can be seen from Fig. 21(b) that with the increase of spring elastic coefficient, the phase differences  $Pd_{1,2}$  and  $Pd_{2,3}$  gradually decrease.

**D. Effects of temperature gradient**

Within Fig. 22, the relationship between the temperature gradient and the system’s amplitude, frequency, and phase difference in the asynchronous mode is plotted, where other system parameters are chosen as  $\bar{K} = 14$ ,  $\bar{k} = 6$ ,  $\bar{\alpha} = -0.2$ ,  $\bar{a}_0 = 0.02$ ,  $\bar{a}_1 = 0.6$ ,  $\bar{\tau} = 0.15$ ,  $v_1^0 = 1$ ,  $v_2^0 = 0$ , and  $v_3^0 = -5$ . As shown in Fig. 22(a), when  $\bar{\beta} < 0.1$ , the system is in the static regime. When  $\bar{\beta} > 0.1$ , the system is in the self-oscillation regime, where amplitude and frequency increase as the temperature gradient increases. The reason is, the greater the temperature gradient, the faster the temperature increases, the more heat is absorbed by the LCE fiber; and then the higher the kinetic energy of the system, the greater the self-oscillation amplitude. Figure 22(b) shows that the system firstly operates in partial synchronous mode. Then, with the increase of  $\bar{\beta}$ , the system evolves into asynchronous mode, and at this point  $Pd_{1,2}$  increases and  $Pd_{2,3}$  decreases.

**E. Effects of the first damping coefficient**

Figure 23 elucidates how the first damping coefficient affects amplitude, frequency, and phase difference in the

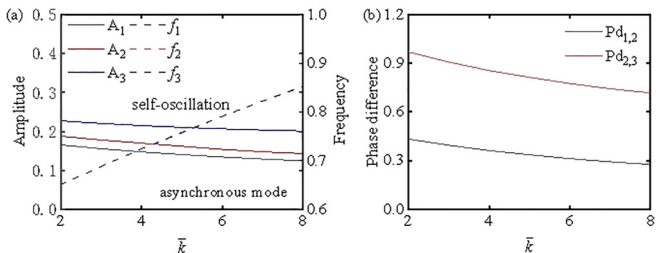


FIG. 21. The effect of spring elastic coefficient on the self-oscillation in asynchronous mode. (a) Variations of amplitude and frequency with different spring elastic coefficients. (b) Variations of phase difference with different spring elastic coefficients.

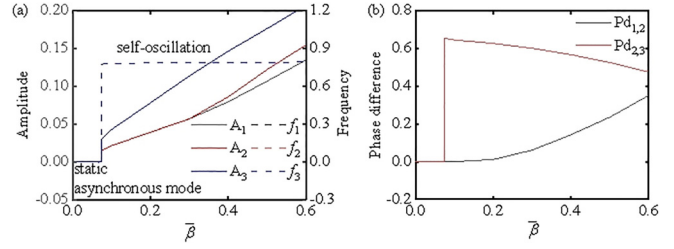


FIG. 22. The effect of temperature gradient on the self-oscillation in asynchronous mode. (a) Variations of amplitude and frequency with different temperature gradients. (b) Variations of phase difference with different temperature gradients.

asynchronous mode, where other system parameters are selected as  $\bar{K} = 14$ ,  $\bar{k} = 6$ ,  $\bar{\alpha} = -0.2$ ,  $\bar{\beta} = 0.6$ ,  $\bar{a}_1 = 0.6$ ,  $\bar{\tau} = 0.15$ ,  $v_1^0 = 1$ ,  $v_2^0 = 0$ , and  $v_3^0 = -5$ . It can be seen from Fig. 23(a) that the system is in the static regime with  $\bar{a}_0 > 0.12$ , while the system is in the self-oscillation regime with  $\bar{a}_0 < 0.12$ . Figure 23(a) shows that an increase in the first damping coefficient can lead to a decrease in the amplitude and frequency of self-oscillation. This is because the greater the first damping coefficient, the larger the damping dissipation, and the smaller the kinetic energy, which results in a smaller amplitude. Figure 23(b) plots the curve of phase differences  $Pd_{1,2}$  and  $Pd_{2,3}$  with the first damping coefficient  $\bar{a}_0$ . Figure 23(b) shows that the system is in the asynchronous mode first, then phase difference  $Pd_{1,2}$  gradually decreases and phase difference  $Pd_{2,3}$  gradually increases as  $\bar{a}_0$  increases.

**F. Effects of the second damping coefficient**

Figure 24 elucidates how the second damping coefficient affects the amplitude, frequency, and phase difference in an asynchronous mode, where other system parameters are selected as  $\bar{K} = 14$ ,  $\bar{k} = 6$ ,  $\bar{\alpha} = -0.2$ ,  $\bar{\beta} = 0.6$ ,  $\bar{a}_0 = 0.02$ ,  $\bar{\tau} = 0.15$ ,  $v_1^0 = 1$ ,  $v_2^0 = 0$ , and  $v_3^0 = -5$ . Figure 24(a) shows that the system is always in the self-oscillation regime, where the amplitude and frequency decrease as the second damping coefficient increases. The reason is, the higher the second damping coefficient, the higher the damping dissipation, and the lower the kinetic energy, which results in a smaller amplitude. Figure 24(b) shows that with the increase of the second damping coefficient, the phase difference between the fibers is basically unchanged.

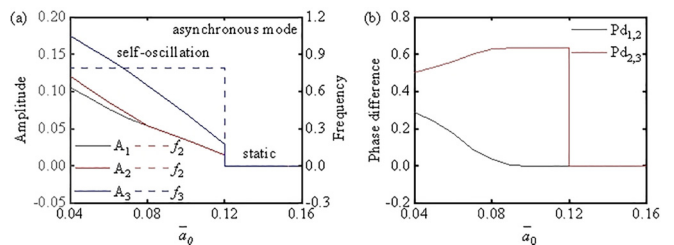


FIG. 23. The effect of the first damping coefficient on the self-oscillation in asynchronous mode. (a) Variations of amplitude and frequency with different first damping coefficients. (b) Variations of phase difference with different first damping coefficients.

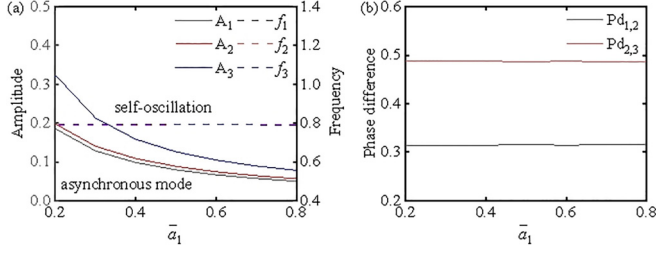


FIG. 24. The effect of the second damping coefficient on the self-oscillation in asynchronous mode. (a) Variations of amplitude and frequency with different second damping coefficients. (b) Variations of phase difference with different second damping coefficients.

### G. Effects of characteristic time

Figure 25 shows the influence of characteristic time on the amplitude, frequency, and phase difference of the self-oscillation, where other system parameters are selected as  $\bar{K} = 14$ ,  $\bar{k} = 6$ ,  $\bar{\alpha} = -0.2$ ,  $\bar{\beta} = 0.6$ ,  $\bar{a}_0 = 0.02$ ,  $\bar{a}_1 = 0.6$ ,  $v_1^0 = 1$ ,  $v_2^0 = 0$ , and  $v_3^0 = -5$ . Figure 25(a) illustrates that under the conditions of  $\bar{\tau} < 0.02$ , the system is always in the static regime, and under the conditions of  $\bar{\tau} > 0.02$ , the system transitions into a self-oscillation regime. It can be seen from Fig. 25(a) that as the characteristic time increases, the amplitude and frequency increase. The reason is, the higher the characteristic time, the more heat energy the LCE fibers absorb, and the more kinetic energy the system has, which results in a higher amplitude. As shown in Fig. 25(b), when  $0.02 < \bar{\tau} < 0.04$ ,  $Pd_{1,2} = 0$ , and  $Pd_{2,3}$  reaches the maximum, the system is in the partial synchronous mode. As the characteristic time increases,  $Pd_{1,2}$  gradually increases, and  $Pd_{2,3}$  gradually decreases, while the system is in the asynchronous mode.

## VII. CONCLUSIONS

Self-exciting coupled oscillators are pervasive in natural phenomena, playing a pivotal role in synchronous and cluster

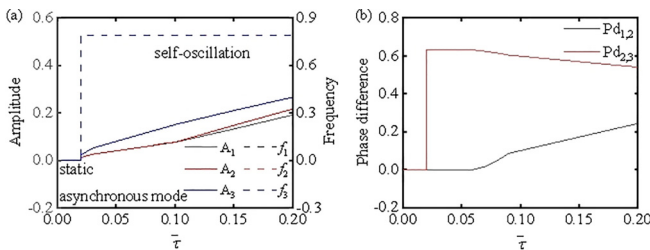


FIG. 25. The effect of characteristic time on the self-oscillation in asynchronous mode. (a) Variations of amplitude and frequency with different characteristic times. (b) Variations of phase difference with different characteristic times.

behaviors. This paper delves into the synchronization modes within a system of three interconnected self-oscillators, which are thermal responsive LCE fibers under linear temperature field. Based on the dynamic LCE model, we derived the governing equations of the coupled system and revealed the mechanisms of self-oscillation. Numerical calculation shows that the self-oscillation is maintained when the damping dissipation and the net work done by LCE fiber tension are dynamically balanced. Three distinct synchronous modes within the system can be obtained: the full synchronous mode, the partial synchronous mode, and the asynchronous mode.

Further calculations show that the coupled LCE-based spring oscillators always develop into the full synchronous self-oscillation when the driving force of the LCE fiber is large. However, when the driving force is low, changing the initial velocity can adjust the synchronous mode. When the initial velocities of the three LCE fibers are equal, the coupled self-oscillating system also can evolve into the full synchronous mode. When the velocity of two LCE fibers is 0 and the velocity of another LCE fiber is larger, the system can evolve into a partial synchronous mode. When the initial velocities of the three LCE fibers are different, the system will develop into an asynchronous mode. For asynchronous mode, when the driving force is small, the system is first a partial synchronous mode, and as the driving force increases, the system gradually evolves into an asynchronous mode.

In addition, we further study the effects of system parameters including LCE and spring elastic coefficient, thermal expansion coefficient, temperature gradient, characteristic time, and the first and the second damping coefficient on the self-oscillation. The amplitude of self-oscillation is positively correlated with the LCE elastic coefficient, temperature gradient, and characteristic time, while the amplitude is negatively correlated with the spring elastic coefficient and the first and the second damping coefficient. The findings of this research offer insights for developing synchronization systems utilizing diverse thermally responsive materials, with practical applications in energy harvesters, soft robotics, medical equipment, and so on. In addition, the system in this paper can be extended to large-scale synchronous systems with a large number of coupled self-oscillators and applied to the field of clustering.

## ACKNOWLEDGMENTS

The authors acknowledge support from the University Natural Science Research Project of Anhui Province (Grant No. 2022AH020029), the National Natural Science Foundation of China (Grant No. 12172001), and Anhui Provincial Natural Science Foundation (Grant No. 2208085Y01).

## APPENDIX: PARAMETER DEFINITIONS

Parameter	Definition
$L_0$	Original length of each LCE fiber
$L_S$	Original length of each spring
$\lambda_1$	Prestretched amount of each LCE fiber
$\lambda_2$	Prestretched amount of each spring
$m_1$	Mass of block 1
$m_2$	Mass of block 2
$m_3$	Mass of block 3
$g$	Gravitational acceleration
$k$	Spring elastic coefficient
$K$	LCE elastic coefficient
$F_{s10}$	Initial elastic forces of the spring 1
$F_{s20}$	Initial elastic forces of the spring 2
$F_{s30}$	Initial elastic forces of the spring 3
$F_{L10}$	Initial elastic forces of the LCE fiber 1
$F_{L20}$	Initial elastic forces of the LCE fiber 2
$F_{L30}$	Initial elastic forces of the LCE fiber 3
$F_{s1}$	Elastic forces of the spring 1
$F_{s2}$	Elastic forces of the spring 2
$F_{s3}$	Elastic forces of the spring 3
$F_{L1}$	Elastic forces of the LCE fiber 1
$F_{L2}$	Elastic forces of the LCE fiber 2
$F_{L3}$	Elastic forces of the LCE fiber 3
$F_{d1}$	Damping force of spring-oscillator 1
$F_{d2}$	Damping force of spring-oscillator 2
$F_{d3}$	Damping force of spring-oscillator 3
$w_1$	Displacement of the mass 1
$w_2$	Displacement of the mass 2
$w_3$	Displacement of the mass 3
$\dot{w}_1$	Velocity of the mass 1
$\dot{w}_2$	Velocity of the mass 2
$\dot{w}_3$	Velocity of the mass 3
$v_1^0$	Initial velocity of the mass 1
$v_2^0$	Initial velocity of the mass 2
$v_3^0$	Initial velocity of the mass 3
$\ddot{w}_1$	Acceleration of the mass 1
$\ddot{w}_2$	Acceleration of the mass 2
$\ddot{w}_3$	Acceleration of the mass 3
$L_1$	Length of LCE fiber 1
$L_2$	Length of LCE fiber 2
$L_3$	Length of LCE fiber 3
$\varepsilon_1$	One-dimensional strain of LCE fiber 1
$\varepsilon_2$	One-dimensional strain of LCE fiber 2
$\varepsilon_3$	One-dimensional strain of LCE fiber 3
$\varepsilon_T$	Heat-induced strain of LCE fibers
$\alpha$	Thermal expansion coefficient
$\beta$	Temperature gradient
$T_{\text{ext}}$	Temperature distribution
$\tau$	Characteristic time
$\rho_c$	Heat capacity
$h$	Heat transfer coefficient
$a_0$	The first damping coefficient
$a_1$	The second damping coefficient

- [1] W. Ding, *Self-Excited Vibration* (Springer, Berlin, Heidelberg, 2010).
- [2] H. Zeng, M. Lahikainen, L. Liu, Z. Ahmed, O. M. Wani, M. Wang, H. Yang, and A. Priimagi, Light-fuelled freestyle self-oscillators, *Nat. Commun.* **10**, 5057 (2019).

- [3] F. Ge, R. Yang, X. Tong, F. Camerel, and Y. Zhao, A multifunctional dye-doped liquid crystal polymer actuator: Light-guided transportation, turning in locomotion, and autonomous motion, *Angew. Chem. Int. Ed.* **57**, 11758 (2018).

- [4] M.-H. Li, P. Keller, B. Li, X. Wang, and M. Brunet, Light-driven side-on nematic elastomer actuators, *Adv. Mater.* **15**, 569 (2003).
- [5] D. J. Preston, H. J. Jiang, V. Sanchez, P. Rothmund, J. Rawson, M. P. Nemitz, W. Lee, Z. Suo, C. J. Walsh, and G. M. Whitesides, A soft ring oscillator, *Sci. Rob.* **4**, 5496 (2019).
- [6] X. Wang, C. F. Tan, K. H. Chan, X. Lu, L. Zhu, S. Kim, and G. W. Ho, In-built thermo-mechanical cooperative feedback mechanism for self-propelled multimodal locomotion and electricity generation, *Nat. Commun.* **9**, 3438 (2018).
- [7] S. Nocentini, C. Parmeggiani, D. Martella, and D. S. Wiersma, Optically driven soft micro robotics, *Adv. Opt. Mater.* **6**, 1800207 (2018).
- [8] L. Charroyer, O. Chiello, and J.-J. Sinou, Self-excited vibrations of a non-smooth contact dynamical system with planar friction based on the shooting method, *Int. J. Mech. Sci.* **144**, 90 (2018).
- [9] Z. Zhang, N. Duan, C. Lin, and H. Hua, Coupled dynamic analysis of a heavily-loaded propulsion shafting system with continuous bearing-shaft friction, *Int. J. Mech. Sci.* **172**, 105431 (2020).
- [10] L. Yang, L. Chang, Y. Hu, M. Huang, Q. Ji, P. Lu, J. Liu, W. Chen, and Y. Wu, An autonomous soft actuator with light-driven self-sustained wavelike oscillation for phototactic self-locomotion and power generation, *Adv. Funct. Mater.* **30**, 1908842 (2020).
- [11] S. Chun, C. Pang, and S. B. Cho, A micropillar-assisted versatile strategy for highly sensitive and efficient triboelectric energy generation under in-plane stimuli, *Adv. Mater.* **32**, e1905539 (2019).
- [12] Y. Kageyama, T. Ikegami, S. Satonaga, K. Obara, H. Sato, and S. Takeda, Light-driven flipping of azobenzene assemblies-sparse crystal structures and responsive behavior to polarized light, *Chem. Eur. J.* **26**, 10759 (2020).
- [13] X. Lu, H. Zhang, G. Fei, B. Yu, X. Tong, H. Xia, and Y. Zhao, Liquid-crystalline dynamic networks doped with gold nanorods showing enhanced photocontrol of actuation, *Adv. Mater.* **30**, e1706597 (2018).
- [14] Z. Liu, M. Qi, Y. Zhu, D. Huang, X. Zhang, L. Lin, and X. Yan, Mechanical response of the isolated cantilever with a floating potential in steady electrostatic field, *Int. J. Mech. Sci.* **161**, 105066 (2019).
- [15] R. Tang, Z. Liu, D. Xu, J. Liu, L. Yu, and H. Yu, Optical pendulum generator based on photomechanical liquid-crystalline actuators, *ACS Appl. Mater. Interfaces* **7**, 8393 (2015).
- [16] D. Zhao and Y. Liu, A prototype for light-electric harvester based on light-sensitive liquid crystal elastomer cantilever, *Energy* **198**, 117351 (2020).
- [17] M. Hua, C. Kim, Y. Du, D. Wu, R. Bai, and X. He, Swaying gel: Chemo-mechanical self-oscillation based on dynamic buckling, *Matter* **4**, 1029 (2021).
- [18] J. Boissonade and P. D. Kepper, Multiple types of spatio-temporal oscillations induced by differential diffusion in the Landolt reaction, *Phys. Chem. Chem. Phys.* **13**, 4132 (2011).
- [19] R. Yoshida, Self-oscillating gels driven by the Belousov-Zhabotinsky reaction as novel smart materials, *Adv. Mater.* **22**, 3463 (2010).
- [20] H. Koibuchi, Bending of thin liquid crystal elastomer under irradiation of visible light: Finsler geometry modeling, *Polymers* **10**, 757 (2018).
- [21] J. Milavec, V. Domenici, B. Zupancic, A. Rešetic, A. Bubnov, and B. Zalar, Deuteron NMR resolved mesogen vs. crosslinker molecular order and reorientational exchange in liquid single crystal elastomers, *Phys. Chem. Chem. Phys.* **18**, 4071 (2016).
- [22] M. Camacho-Lopez, H. Finkelmann, P. Palffy-Muhoray, and M. Shelley, Fast liquid-crystal elastomer swims into the dark, *Nat. Mater.* **3**, 307 (2004).
- [23] A. Bubnov, V. Domenici, V. Hamplová, M. Kašpar, and B. Zalar, First liquid single crystal elastomer containing lactic acid derivative as chiral co-monomer: Synthesis and properties, *Polymer* **52**, 4490 (2011).
- [24] Y. Wang, J. Liu, and S. Yang, Multi-functional liquid crystal elastomer composites, *Appl. Phys. Rev.* **9**, 011301 (2022).
- [25] Y. Hu, Q. Ji, M. Huang, L. Chang, C. Zhang, G. Wu, B. Zi, N. Bao, W. Chen, and Y. Wu, Light-driven self-oscillating actuators with phototactic locomotion based on black phosphorus heterostructure, *Angew. Chem. Int. Ed.* **60**, 20511 (2021).
- [26] A. Rešetic, J. Milavec, V. Domenici, B. Zupancic, A. Bubnov, and B. Zalar, Stress-strain and thermomechanical characterization of nematic to smectic A transition in a strongly-crosslinked bimesogenic liquid crystal elastomer, *Polymer* **158**, 96 (2018).
- [27] Q. Shen, S. Trabia, T. Stalbaum, V. Palmre, K. Kim, and I.-K. Oh, A multiple-shape memory polymer-metal composite actuator capable of programmable control, creating complex 3D motion of bending, twisting, and oscillation, *Sci. Rep.* **6**, 24462 (2016).
- [28] J. Wu, S. Yao, H. Zhang, W. Man, Z. Bai, F. Zhang, X. Wang, D. Fang, and Y. Zhang, Liquid crystal elastomer metamaterials with giant biaxial thermal shrinkage for enhancing skin regeneration, *Adv. Mater.* **33**, 2170356 (2021).
- [29] L. L. Ma, C. Liu, S. Wu, P. Chen, Q. Chen, J. Qian, S. Ge, Y. Wu, W. Hu, and Y. Lu, Programmable self-propelling actuators enabled by a dynamic helical medium, *Sci. Adv.* **7**, 32 (2021).
- [30] R. Zheng, L. Ma, W. Feng, J. Pan, Z. Wang, Z. Chen, Y. Zhang, C. Li, P. Chen, H. K. Bisoyi *et al.*, Autonomous self-sustained liquid crystal actuators enabling active photonic applications, *Adv. Funct. Mater.* **33**, 2301142 (2023).
- [31] Y. Cui, Y. Yin, C. Wang, K. Sim, Y. Li, C. Yu, and J. Song, Transient thermo-mechanical analysis for bimorph soft robot based on thermally responsive liquid crystal elastomers, *Appl. Math. Mech.* **40**, 943 (2019).
- [32] Y. Guo, N. Liu, Q. Cao, X. Cheng, P. Zhang, Q. Guan, W. Zheng, G. He, and J. Chen, Photothermal diol for NIR-responsive liquid crystal elastomers, *ACS Appl. Polym. Mater.* **4**, 6202 (2022).
- [33] Y. H. Na, Y. Aburaya, H. Orihara, and K. Hiraoka, Measurement of electrically induced shear strain in a chiral smectic liquid-crystal elastomer, *Phys. Rev. E* **83**, 061709 (2011).
- [34] Noorjahan, S. Pathak, K. Jain, and R. Pant, Improved magnetoviscoelasticity of cross-linked PVA hydrogels using magnetic nanoparticles, *Colloids Surf. A* **539**, 273 (2018).
- [35] J. M. Haberl, A. Sánchez-Ferrer, A. M. Mihut, H. Dietsch, A. M. Hirt, and R. Mezzenga, Liquid-crystalline elastomer-nanoparticle hybrids with reversible switch of magnetic memory, *Adv. Mater.* **25**, 1787 (2013).
- [36] C. Ahn, K. Li, and S. Cai, Light or thermally powered autonomous rolling of an elastomer rod, *ACS Appl. Mater. Interfaces* **10**, 25689 (2018).
- [37] A. Bazir, A. Baumann, F. Ziebert, and I. M. Kulić, Dynamics of fiberoids, *Soft Matter* **16**, 5210 (2020).

- [38] Y. Kim, J. van der Berg, and A. J. Crosby, Autonomous snapping and jumping polymer gels, *Nat. Mater.* **20**, 1695 (2021).
- [39] A. H. Gelebart, D. Mulder, M. Varga, A. Konya, G. Vantomme, E. Meijer, and R. Selinger, Making waves in a photoactive polymer film, *Nature (London)* **546**, 632 (2017).
- [40] A. S. Kuenstler, Y. Chen, P. Bui, H. Kim, A. DeSimone, L. Jin, and R. C. Hayward, Blueprinting photothermal shape-morphing of liquid crystal elastomers, *Adv. Mater.* **32**, e2000609 (2020).
- [41] D. Ge, Y. Dai, and K. Li, Self-sustained Euler buckling of an optically responsive rod with different boundary constraints, *Polymers* **15**, 316 (2023).
- [42] R. K. Manna, O. E. Shklyae, and A. C. Balazs, Chemical pumps and flexible sheets spontaneously form self-regulating oscillators in solution, *Proc. Natl. Acad. Sci. USA* **118**, e2022987118 (2021).
- [43] Z. Li, N. V. Myung, and Y. Yin, Light-powered soft steam engines for self-adaptive oscillation and biomimetic swimming, *Sci. Rob.* **6**, eabi4523 (2021).
- [44] S. Serak, N. Tabiry, R. Vergara, T. J. White, R. A. Vaia, and T. J. Bunning, Liquid crystalline polymer cantilever oscillators fueled by light, *Soft Matter* **6**, 779 (2010).
- [45] L. Zhou, Y. Dai, J. Fang, and K. Li, Light-powered self-oscillation in liquid crystal elastomer auxetic metamaterials with large volume change, *Int. J. Mech. Sci.* **254**, 108423 (2023).
- [46] J. Liu, J. Zhao, H. Wu, Y. Dai, and K. Li, Self-oscillating curling of a liquid crystal elastomer beam under steady light, *Polymers* **15**, 344 (2023).
- [47] Q. He, Z. Wang, Y. Wang, Z. Wang, C. Li, R. Annapooranan, J. Zeng, R. Chen, and S. Cai, Electrospun liquid crystal elastomer microfiber actuator, *Sci. Rob.* **6**, eabi9704 (2021).
- [48] Y. Yu, C. Du, K. Li, and S. Cai, Controllable and versatile self-motivated motion of a fiber on a hot surface, *Extreme Mech. Lett.* **57**, 101918 (2022).
- [49] D. L. Ge, Y. T. Dai, and K. Li, Light-powered self-spinning of a button spinner, *Int. J. Mech. Sci.* **238**, 107824 (2023).
- [50] Q. Cheng, W. Cheng, Y. Dai, and K. Li, Self-oscillating floating of a spherical liquid crystal elastomer balloon under steady illumination, *Int. J. Mech. Sci.* **241**, 107985 (2023).
- [51] C. M. Yakacki, M. Saed, D. P. Nair, T. Gong, S. M. Reed, and C. N. Bowman, Tailorable and programmable liquid-crystalline elastomers using a two-stage thiol-acrylate reaction, *RSC Adv.* **5**, 18997 (2015).
- [52] Y. Wang, R. Yin, L. Jin, M. Liu, Y. Gao, J. Raney, and S. Yang, 3D-printed photoresponsive liquid crystal elastomer composites for free-form actuation, *Adv. Funct. Mater.* **33**, 2210614 (2023).
- [53] Y. Wang, A. Dang, Z. Zhang, R. Yin, Y. Gao, L. Feng, and S. Yang, Repeatable and reprogrammable shape morphing from photoresponsive gold nanorod/liquid crystal elastomers, *Adv. Mater.* **32**, 2004270 (2020).
- [54] M. Parrany, Nonlinear light-induced vibration behavior of liquid crystal elastomer beam, *Int. J. Mech. Sci.* **136**, 179 (2018).
- [55] M. Warner and E. M. Terentjev, *Liquid Crystal Elastomers* (Oxford University Press, Oxford, UK, 2007).
- [56] S. Strogatz, Synchronization: A universal concept in nonlinear science, *Phys. Today* **56** (1), 47 (2003).
- [57] T. Vicsek and A. Zafeiris, Collective motion, *Phys. Rep.* **517**, 71 (2012).
- [58] S. Boccaletti, The synchronized dynamics of complex systems, *Monograph.* **6**, 1 (2008).
- [59] K. P. O’Keeffe, H. Hong, and S. H. Strogatz, Oscillators that sync and swarm, *Nat. Commun.* **8**, 1504 (2017).
- [60] Y. Yu, Synchronized dancing under light, *Nat. Mater.* **20**, 1594 (2021).
- [61] M. Bennett, M. F. Schatz, and H. Rockwood, Huygens’s clocks, *Proc. R. Soc. A* **458**, 563 (2002).
- [62] J. P. Ramirez, L. A. Olvera, and H. Nijmeijer, The sympathy of two pendulum clocks: Beyond Huygens’ observations, *Sci. Rep.* **6**, 23580 (2016).
- [63] A. Bayani, S. Jafari, H. Azarnoush, F. Nazarimehr, S. Boccaletti, and M. Perc, Explosive synchronization dependence on initial conditions: The minimal Kuramoto model, *Chaos, Solitons Fractals* **169**, 113243 (2023).
- [64] C. Wang, Dynamic behavior analysis and robust synchronization of a novel fractional-order chaotic system with multiwing attractors, *J. Math.* **2021**, 6684906 (2021).
- [65] S. Yan, J. Wang, E. Wang, Q. Wang, X. Sun, and L. Li, A four-dimensional chaotic system with coexisting attractors and its backstepping control and synchronization, *Integration* **91**, 67 (2023).
- [66] F. Parastesh, K. Rajagopal, S. Jafari, M. Perc, and E. Schöll, Blinking coupling enhances network synchronization, *Phys. Rev. E* **105**, 054304 (2022).
- [67] D. Levis, I. Pagonabarraga, and A. Díaz-Guilera, Synchronization in dynamical networks of locally coupled self-propelled oscillators, *Phys. Rev. X* **7**, 011028 (2017).
- [68] G. Vantomme, L. C. M. Elands, A. H. Gelebart, E. W. Meijer, A. Y. Pogromsky, H. Nijmeijer, and D. J. Broer, Coupled liquid crystalline oscillators in Huygens’ synchrony, *Nat. Mater.* **20**, 1702 (2021).
- [69] K. Li, B. Zhang, Q. Cheng, Y. Dai, and Y. Yu, Light-fueled synchronization of two coupled liquid crystal elastomer self-oscillators, *Polymers* **15**, 2886 (2023).
- [70] C. Du, Q. Cheng, K. Li, and Y. Yu, Self-sustained collective motion of two joint liquid crystal elastomer spring oscillator powered by steady illumination, *Micromachines* **13**, 271 (2022).
- [71] Y. Wang, J. Sun, W. Liao, and Z. Yang, Liquid crystal elastomer twist fibers towards rotating microengines, *Adv. Mater.* **34**, 2107840 (2022).
- [72] T. Nagele, R. Hoche, W. Zinth, and J. Wachtveitl, Femtosecond photoisomerization of *cis*-azobenzene, *Chem. Phys. Lett.* **272**, 489 (1997).
- [73] L. Zhou, C. Du, W. Wang, and K. Li, A thermally-responsive fiber engine in a linear temperature field, *Int. J. Mech. Sci.* **225**, 107391 (2022).
- [74] L. B. Braun, T. Hessberger, E. Pütz, C. Müller, F. Giesselmann, C. A. Serra, and R. Zentel, Actuating thermo- and photo-responsive tubes from liquid crystalline elastomers, *J. Mater. Chem. C* **6**, 9093 (2018).
- [75] Y. C. Fung and D. C. Drucker, Foundation of solid mechanics, *J. Appl. Mech.* **33**, 238 (1966).
- [76] V. S. R. Jampani, R. H. Volpe, K. R. de Sousa, J. F. Machado, C. M. Yakacki, and J. P. F. Lagerwall, Liquid crystal elastomer shell actuators with negative order parameter, *Sci. Adv.* **5**, eaaw2476 (2019).
- [77] V. Lee and K. Bhattacharya, Actuation of cylindrical nematic elastomer balloons, *J. Appl. Phys.* **129**, 114701 (2021).